Volume 17
Number 17
6 May 2026
Pages 8313–8808

Chemical Science

rsc.li/chemical-science

ISSN 2041-6539

ROYAL SOCIETY
OF **CHEMISTRY**

EDGE ARTICLE
Montree Sawangphruk *et al.*
Solvation-driven interphase engineering and mechanical failure pathways in large-scale anode-free lithium metal batteries

Chemical Science

EDGE ARTICLE

View Article Online
View Journal | View Issue

Cite this: *Chem. Sci.*, 2026, **17**, 8453

All publication charges for this article have been paid for by the Royal Society of Chemistry

Received 3rd January 2026
Accepted 23rd March 2026

DOI: 10.1039/d6sc00025h

rsc.li/chemical-science

Solvation-driven interphase engineering and mechanical failure pathways in large-scale anode-free lithium metal batteries

Nattanon Joraleechanchai, Nuttida Matkhaw, Thitiphum Sangsanit,
Worapol Tejangkura and Montree Sawangphruk *

Anode-free lithium–metal batteries promise ultrahigh energy density but remain limited by unstable interfaces and safety concerns. Here, we demonstrate that fluorinated-ether solvation chemistry directly dictates interphase formation, thermal behavior, and performance in large-format Cu||NMC90 cells. We reveal that introducing 1,1,2,2-tetrafluoroethyl 2,2,3,3-tetrafluoropropyl ether (TTE) into a localized high-concentration electrolyte restructures the Li^+ solvation shell into a previously unreported PF_6^--dominated coordination environment in practical cylindrical cells. This anion-rich solvation promotes preferential PF_6^- reduction and yields a dense LiF-rich solid-electrolyte interphase, as verified by nuclear magnetic resonance, X-ray photoelectron spectroscopy, and differential electrochemical mass spectrometry. The optimized electrolyte enables non-flammable behavior and high efficiency in 18650-format anode-free cells, achieving 278–308 Wh kg^{-1} at the cell level (380–402 Wh kg^{-1} at the jelly-roll level), nearly 100% coulombic efficiency, and compliance with UN38.3 impact-safety standards. Importantly, we identify lithium-plating-induced mechanical expansion—not interfacial instability—as the dominant failure pathway, establishing a direct link between molecular solvation structure and macroscopic structural integrity. These findings define solvation-driven interphase engineering as a practical route toward safe, high-energy anode-free lithium–metal batteries.

1. Introduction

Anode-free lithium metal batteries (LMBs) have emerged as promising next-generation energy storage systems due to their exceptional gravimetric and volumetric energy densities, achieved by eliminating the conventional graphite anode and its associated inactive materials.[1–6] In this minimalist configuration, lithium is plated directly onto the current collector during the first charge, reducing cell weight and simplifying architecture. However, despite these advantages, anode-free LMBs suffer from uneven lithium deposition, dendritic growth, and unstable electrode–electrolyte interfaces, leading to rapid capacity fade, low coulombic efficiency, and severe safety concerns.[7–9] These limitations hinder not only laboratory performance but also large-scale manufacturability and long-term reliability.

Among mitigation strategies, electrolyte engineering has proven the most direct and effective route to stabilize both lithium morphology and interfacial chemistry.[7–10] The electrolyte governs the solvation environment of Li^+ ions, which dictates reduction pathways and the composition of the resulting solid electrolyte interphase (SEI). High-concentration electrolytes (HCEs), characterized by strong Li^+–anion interactions, produce anion-rich solvation structures where PF_6^- participates directly in Li^+ coordination.[10] This leads to preferential anion reduction and the formation of inorganic-rich SEIs (LiF, Li_2O, Li_2CO_3) with high mechanical strength and ionic conductivity—effectively suppressing dendrite growth. However, their high viscosity, poor wettability, and cost restrict large-scale use, particularly in 18650-format cells, which demand uniform electrolyte distribution through thick electrodes.[11]

To address these trade-offs, localized high-concentration electrolytes (LHCEs) have been introduced by adding non-coordinating diluents that preserve the local HCE solvation structure while reducing viscosity and cost.[12–14] Among them, the fluorinated ether 1,1,2,2-tetrafluoroethyl 2,2,3,3-tetrafluoropropyl ether (TTE) stands out for its high oxidative stability, non-flammability, and weak solvating nature. The electron-withdrawing $-CF_3$ groups in TTE suppress oxidative decomposition and combustion, enhancing safety under mechanical and thermal stress. Yet, the molecular mechanism by which TTE reorganizes Li^+ solvation and influences SEI formation in large-format anode-free cells remains unclear.

Centre of Excellence for Energy Storage Technology (CEST), Department of Chemical and Biomolecular Engineering, School of Energy Science and Engineering, Vidyasirimedhi Institute of Science and Technology, Rayong, 21210, Thailand. E-mail: montree.s@vistec.ac.th

In this study, we elucidate how a fluorinated ether diluent modulates solvation chemistry, interfacial reactions, and mechanical stability in 18650-type anode-free LMBs. Using NMR, XPS, and DEMS, we show that TTE induces an anion-rich solvation shell, promoting preferential PF_6^- reduction and the formation of a LiF-dominated SEI. This interphase enhances coulombic efficiency, suppresses side reactions, and ensures non-flammable operation verified by the UN38.3 impact test. Crucially, we reveal that ultimate cell failure arises from mechanical rupture driven by volumetric expansion, linking molecular solvation design to macroscopic structural integrity.

2. Experimental section

2.1 Materials characterization

The all as-received solvents including Fluoroethylene carbonate (FEC), diethyl carbonate (DEC), and TTE purchased from Shandong Gelon Lib Co. (China) were verified prior to use *via* ^{1}H Nuclear Magnetic Resonance (NMR) spectroscopy as shown in Fig. S1, S2 and S3, respectively.

2.2 Electrolyte preparation

Lithium hexafluorophosphate ($LiPF_6$) salt was purchased from Shandong Gelon Lib Co. (China). Prior to use, all solvents were subjected to drying over 4 Å molecular sieves overnight to remove trace moisture. A solution of 1.2 M $LiPF_6$ in a mixture of FEC and DEC (25 : 75 by volume) was formulated and designated as the baseline electrolyte. The non-flammable experimental electrolytes were then prepared by incorporating various volume ratios of TTE into this baseline formulation. All procedures involving electrolyte preparation and cell assembly were conducted under an Argon-filled atmosphere in glove box, where oxygen and moisture levels were maintained below 0.1 ppm.

2.3 Fabrication of 18650 cylindrical cells

All materials including $LiNi_{0.90}Co_{0.05}Mn_{0.05}O_2$ (NMC90), prelithiation agent Li_2NiO_2, carbon black (Super P), and polyvinylidene fluoride (PVDF) binder were purchased from Shandong Gelon Lib Co. (China). The fabrication of 18650 cylindrical cells was performed in a dry room with a dew point maintained at −40 °C for cell assembly and −55 °C for the electrolyte injection process. All powdered materials, including the active cathode materials (NMC90), prelithiation agent Li_2NiO_2, carbon black (Super P), and PVDF binder, were dried in a vacuum oven at 80 °C for 24 h before use. The cathode slurry was prepared by homogenizing a mixture of the active material, carbon black, and PVDF binder in a weight ratio of 95.2 : 2.4 : 2.4 in an *N*-methyl-2-pyrrolidone (NMP) solvent using a planetary vacuum mixer. The final slurry had a solid content of approximately 67.6%. The resulting slurry was then cast onto aluminum foil using a roll-to-roll automatic coating system equipped with an integrated 120 °C drier. The final thickness of the coated cathode electrodes was 218 μm, with a mass loading of approximately 18.8 mg cm^{-2}. The copper foil with 12 μm thickness was used as anode.

2.4 Fabrication of CR2032 coin cells

Anode-free half-cells were assembled in CR2032-type coin cell. The cathode material used was identical to that prepared for the cylindrical cells. The cathodes were punched into 14 mm diameter discs. The coin cells were constructed by sequentially stacking the cathode disc, a polyethylene (PE) separator, and a copper foil disc, which served as the anode current collector. All coin cell assembly was performed inside an argon-filled glove box (MBraun, Germany) with oxygen and water concentrations maintained below 0.1 ppm.

2.5 Electrochemical characterization

The electrochemical performance of the 18650 cylindrical full cells was evaluated at ambient temperature using a Neware battery test system (China). Prior to performance evaluation, all cells underwent initial formation cycles, which were conducted at a C/10 charging rate and a C/2 discharging rate and within a voltage window of 3.0 V to 4.3 V for 2 cycles. Cycling stability was evaluated by charging the cells at a C/5 charging and C/2 discharging rate between 3.0 V and 4.3 V.

2.6 Electrochemical impedance spectroscopy (EIS) measurement

EIS measurements were conducted using CR2032-type coin cells assembled in a Cu||NMC90 + Li_2NiO_2 configuration. The impedance spectra were collected at 50% state of charge (SoC) to ensure comparable interfacial conditions across different electrolyte formulations. Prior to measurement, the cells were allowed to rest for 2 h to reach electrochemical equilibrium. Temperature-dependent EIS measurements were performed at 30, 20, 10, 0, and −10 °C using a potentiostat/galvanostat equipped with an impedance module. The impedance response was recorded over a frequency range of 1 MHz to 0.1 Hz with a sinusoidal voltage perturbation of 1 mV. The obtained Nyquist plots were fitted using an equivalent circuit model to extract the ohmic resistance (R_s), contact resistance ($R_{CONTACT}$) interfacial resistance (R_{SEI}), and charge-transfer resistance (R_{CT}). The temperature dependence of resistance was further analyzed using an Arrhenius equation to determine the apparent activation energy associated with the interfacial charge-transfer process.[15]

$$\frac{1}{R} = A\mathrm{e}^{-\frac{E_a}{k_B T}} \tag{1}$$

R represents the resistance associated with Li^+ transport across different elements. E_a corresponds to the activation energy required for lithium ions to migrate through hopping sites within the SEI. k_B is the Boltzmann constant, *T* denotes the absolute temperature, and *A* is a proportionality constant.

2.7 Post-mortem analysis

For post-mortem studies, the 18650 cells were disassembled inside an argon-filled glove box using an 18650-disassembly machine. The cycled electrodes were rinsed with dimethyl carbonate (GELON, China) to remove residual electrolyte salt and solvents. The cleaned samples were then dried within the glove box before characterization.

Surface chemical analysis was performed using X-ray Photoelectron Spectroscopy (XPS) on a JEOL JPS-9010 MC instrument with a monochromatic Mg-Kα radiation source ($h\nu = 1253.6$ eV). Spectra were acquired at 12 kV and 25 mA under a high vacuum (10^{-7} Pa). To investigate the layered structure of the interphase, XPS depth profiling was achieved through sequential Ar^+ etching steps, each with a duration of 20 s. Binding energies were calibrated using the adventitious carbon C 1s peak at 284.8 eV or the Li_2O O 1s peak at 528.5 eV. To prevent atmospheric exposure, all samples were transferred from the glove box to the XPS chamber using an air-sensitive transfer holder.

2.8 Differential electrochemical mass spectrometry (DEMS)

In situ analysis of gaseous evolution during electrochemical cycling was performed using a Hiden Analytical (UK) HPR-40 DEMS system controlled by QGA professional software. For the measurement, a test-tube contained 18650-type jelly roll was utilized inside an argon-filled glovebox. Volatile species were ionized using an electron energy of 70 eV with an emission current of 500 μA, and the high-vacuum chamber was maintained at a working pressure below 5×10^{-8} torr. The experiment commenced with a 2 h background monitoring period to establish a stable baseline. The cell was then charged under formation protocol and C/10 a constant-current (CC)-charge-CC discharge, and follow by a CC protocol to 4.7 V; this charging profile incorporated 1 h potentiostatic holds at 0.1 V intervals between 4.2 V and 4.7 V to observe gas evolution under specific voltage conditions.

2.9 Nuclear magnetic resonance (NMR) spectroscopy

To quantify the concentration of soluble degradation products in the liquid electrolyte, an internal standard method was employed. Following the completion of electrochemical cycling or abuse tests, electrolyte was harvested from the test tube contained jelly rolls. A 70 μL aliquot of the extracted electrolyte was then diluted in a solution of deuterated dimethyl sulfoxide (DMSO-d_6) which contained 1,4-dinitrobenzene (1 mg mL^{-1}) as a calibrated internal standard. The final volume of the mixture for analysis was 700 μL. The resulting solutions were then analyzed using ^1H-NMR spectroscopy with the instrumentation described previously. The behavior of Li^+ and PF_6^- in electrolyte were investigated by measuring the diffusion coefficients (D) utilizing ^7Li and ^{19}F Pulsed-Field Gradient (PFG) NMR, respectively, with the 2D Diffusion-Ordered Spectroscopy (DOSY) technique. Diffusion coefficients were calculated by fitting the decay of the NMR signal echo height as a function of the applied gradient strength, using the Stejskal–Tanner equation. The fitting procedure was performed using Bruker's Topspin and Dynamics Center software. To isolate the sample from the deuterium lock solvent and prevent chemical interference, coaxial NMR tubes (ATS Life Sciences Wilmad, USA) were employed for all measurements. For each analysis, 260 μL of the post-cycled electrolyte was placed in the outer tube, while the inner tube contained 220 μL of a 1 M $LiPF_6$ solution in DMSO-d_6. This inner solution served as both the deuterium lock for the spectrometer and an external chemical shift reference for the reference peak (−1.00 ppm). This coaxial arrangement prevented direct mixing of the sample and reference solutions, ensuring chemical stability and enabling accurate kinetic analysis.

2.10 Viscosity measurement

The dynamic viscosity of the electrolyte solutions was measured using a Discovery HR-20 rheometer equipped with a parallel plate. For each measurement, approximately 3.5 mL of the sample was loaded. The shear rate was increased exponentially from 10 to 100 s^{-1} over 25 steps. A duration of 30 s was maintained at each step to ensure steady-state flow conditions before the torque was measured to calculate the dynamic viscosity.

2.11 Gas chromatography-mass spectrometry (GC-MS)

To qualitatively identify soluble degradation byproducts, liquid electrolyte samples were analyzed using a PerkinElmer Clarus SQ8T-Clarus680GC Gas Chromatography-Mass Spectrometry system. Following chromatographic separation, the mass spectra of the eluted compounds were referenced against the NIST Mass Spectral Library, and the species with the highest match score was selected for identification.

A temperature-programmed protocol was utilized to ensure optimal resolution of the volatile decomposition products. The method consisted of the following steps: an initial temperature holds at 60 °C, a ramp of 25 °C per minute to 180 °C, an intermediate hold at 180 °C for 2 min, and a final ramp to 280 °C, where the temperature was maintained for an additional 2 min. This controlled heating profile was designed to achieve effective volatilization and separation of all electrolyte components and their byproducts while ensuring high analytical reproducibility for direct comparison between samples.

2.12 UN38.3 impact test (T6)

A safety and abuse test was conducted in accordance with the UN38.3 (T6) standard. The impact test was performed by placing a 16 mm diameter steel column on the center of the cell, onto which a 9.1 kg mass was dropped from a height of 610 mm. The test was conducted using the Guangdong bell experiment equipment's tester.

3. Results and discussion

3.1 Flammability suppression by fluorinated ether diluent (TTE)

The intrinsic flammability of liquid electrolytes presents a major safety limitation for high-energy-density lithium batteries. To quantitatively evaluate flame resistance, ignition time and self-extinguishing time (SET) were measured using a standardized straw flame test, as illustrated in Fig. 1. The results show that increasing the concentration of TTE markedly enhances flame retardancy, evidenced by prolonged ignition times and reduced SET values. At higher TTE contents, the electrolyte transitions from flammable to non-flammable

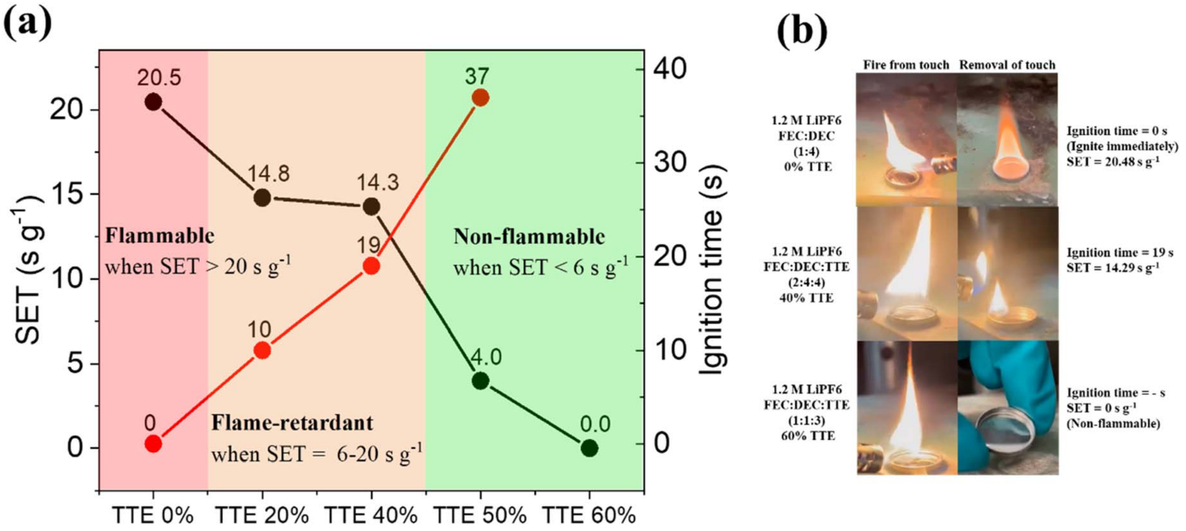

Fig. 1 Flammability behavior of localized high-concentration electrolytes containing the fluorinated ether diluent TTE. (a) Self-extinguishing time (SET, left axis) and ignition time (right axis) as a function of TTE volume fraction in 1.2 M $LiPF_6$ in FEC : DEC (1 : 4). Shaded regions denote safety classifications: flammable (SET > 20 s g^{-1}), flame-retardant (6 ≤ SET ≤ 20 s g^{-1}), and non-flammable (SET < 6 s g^{-1}). Increasing TTE content progressively suppresses flammability, rendering the electrolyte completely non-flammable at ≥ 50 vol% TTE. (b) Representative photographs showing flame responses of electrolytes with 0%, 40%, and 60% TTE during and after exposure. The baseline FEC : DEC (1 : 4) electrolyte ignites immediately and sustains burning, the 40% TTE formulation exhibits delayed ignition and self-extinguishing behavior, and the 60% TTE electrolyte shows no ignition upon flame contact, confirming its non-flammable character.

behavior, demonstrating the critical role of the fluorinated ether diluent in suppressing combustion and improving thermal safety.

The conventional electrolyte (1.2 M $LiPF_6$ in FEC : DEC (1 : 4), 0% TTE) ignited instantly upon flame contact and sustained combustion, exhibiting a SET of approximately 20.5 s g^{-1}, as shown in Fig. 1a and b. In sharp contrast, the incorporation of TTE markedly reduced flammability.[16] Electrolytes containing 20% and 40% TTE still burned but displayed delayed ignition times of 10 and 19 s, respectively, with SET values reduced to 14.8 and 14.3 s g^{-1}—both within the flame-retardant regime.[17] Remarkably, the 50% TTE formulation exhibited a prolonged ignition delay of 37 s and an SET of only 4 s g^{-1}, while the 60% TTE electrolyte showed no visible flame propagation throughout testing. According to standard safety classifications (SET < 6 s g^{-1} for non-flammable, 6–20 s g^{-1} for flame-retardant, and > 20 s g^{-1} for flammable materials),[17] the 50% and 60% TTE electrolytes are definitively categorized as non-flammable, underscoring the strong flame-suppressing capability of the fluorinated ether diluent.

3.2 Solvation structure evolution induced by TTE

The physicochemical behavior of the electrolyte provides molecular-level insight into how fluorinated ether diluents restructure the solvation environment and influence ion transport. As shown in Fig. 2a, the ^{7}Li NMR spectra display a continuous upfield shift with increasing TTE concentration, reflecting a change in the local electronic environment of Li^+ ions. This chemical shift evolution indicates stronger electrostatic interactions between Li^+ and nearby electronegative species, consistent with the progressive replacement of solvent-coordinated Li^+ by anion-coordinated complexes. In parallel, the ^{19}F NMR spectra (Fig. 2b) exhibit distinct upfield movements of the PF_6^- doublet peaks, signifying a shift of PF_6^- from a free-ion state to direct coordination within the Li^+ solvation sheath.[18,19]

The simultaneous upfield shifts in both ^{7}Li and ^{19}F resonances provide compelling evidence for the formation of contact ion pairs (CIPs) and aggregated ion complexes (AGGs), hallmarks of a LHCE environment.[19,20] In this configuration, the TTE, which is weakly solvating and chemically inert, selectively excludes itself from the Li^+ coordination sphere. This exclusion enhances the participation of PF_6^- in the primary solvation shell as illustrated in Fig. 2e, giving rise to an anion-rich solvation structure. Such structural reorganization is critical because it governs the initial reduction pathway during electrochemical cycling, promoting preferential anion decomposition and thus the formation of an inorganic, LiF-dominated interphase on the electrode surface.

Macroscopic transport properties corroborate this microscopic picture. As TTE concentration increases, the electrolyte viscosity rises steadily (Fig. 2c), reflecting enhanced ion association and reduced solvent mobility. The corresponding lithium-ion diffusion coefficients (Fig. 2d) decrease from 1.875 × 10^{-10} m^2 s^{-1} in the baseline FEC: DEC system to 0.141 × 10^{-10} m^2 s^{-1} in the most fluorinated composition. This reduction is a natural outcome of the stronger ion–ion interactions within the clustered solvation network. Nevertheless, the moderate decline in D_{Li^+} is offset by improved interfacial stability and safety, indicating that optimized solvation chemistry rather than bulk ionic conductivity dominates overall electrochemical performance.

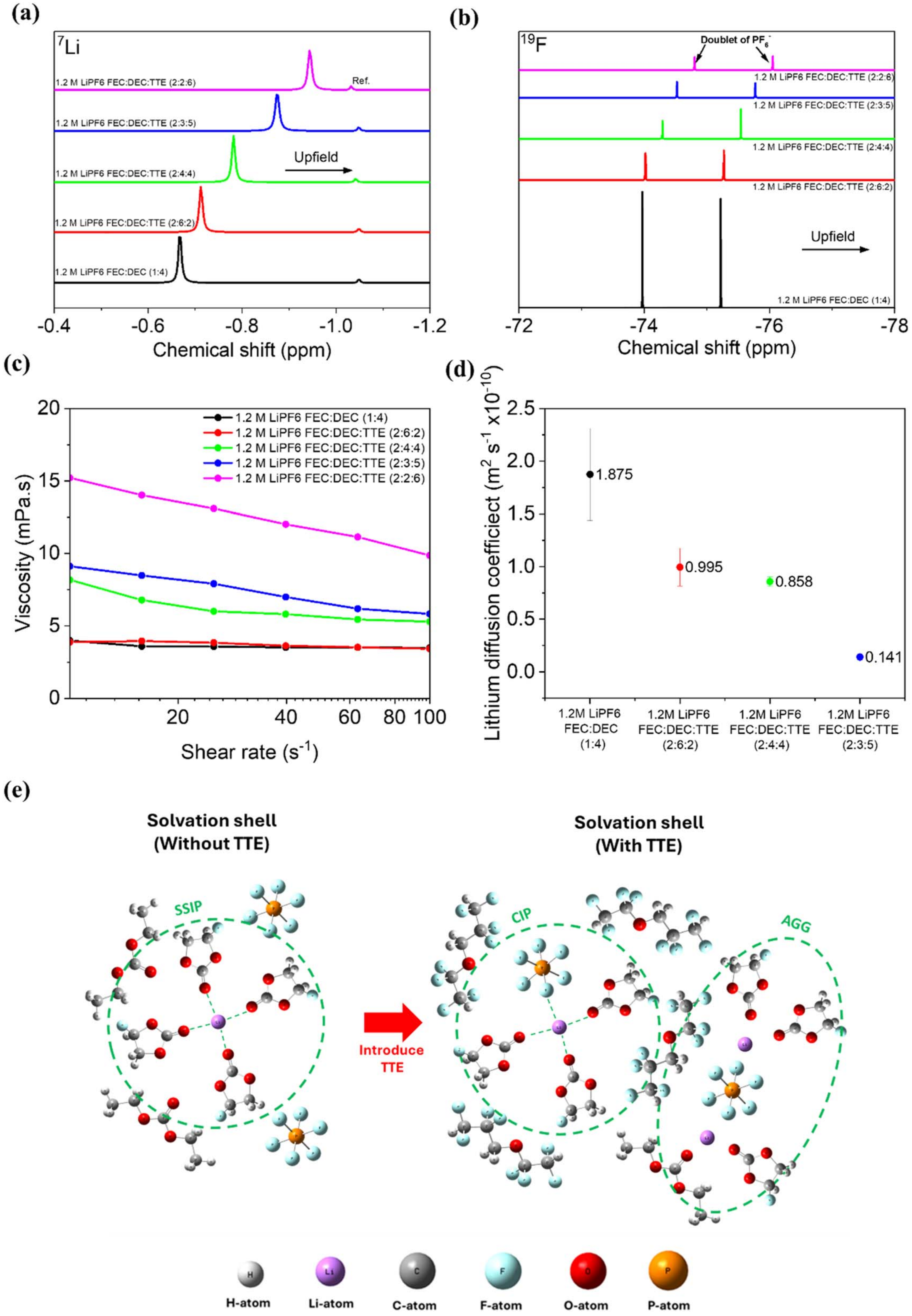

Fig. 2 Physicochemical and spectroscopic characterization of localized high-concentration electrolytes containing the fluorinated ether diluent TTE. (a) ^{7}Li and (b) ^{19}F NMR spectra of electrolytes with varying FEC : DEC : TTE volume ratios, showing systematic upfield chemical shifts indicative of stronger Li^+–anion coordination and the formation of contact ion pairs in TTE-rich formulations. (c) Viscosity profiles of the electrolytes as a function of shear rate, demonstrating increased viscosity with higher TTE content due to reduced solvent mobility. (d) Lithium-ion diffusion coefficients derived from pulsed-field-gradient NMR measurements, revealing progressively slower Li^+ transport in highly fluorinated compositions. (e) Illustration comparing the solvation structures of electrolytes with and without TTE.

3.3 Electrochemical baseline in anode-free coin cells

To establish the electrochemical baseline, anode-free NMC90 + Li_2NiO_2 coin cells were first evaluated using electrolytes with varying TTE concentrations. In this system, Li_2NiO_2 serves as a pre-lithiated additive providing a supplemental Li source, as reported previously.[21] The initial charge–discharge profiles (Fig. S4a) and corresponding differential capacity (dQ/dV) plots (Fig. S4b) reveal the typical redox transitions of Ni^{2+}/Ni^{4+} within the layered oxide framework. The evolution of dQ/dV peaks with cycling (Fig. 3) illustrates progressive interfacial stabilization in TTE-containing electrolytes. At a cycling rate of 0.2C for charge and 0.5C for discharge,[22,23] cells with higher TTE fractions maintain superior capacity retention (Fig. S4c and d) and exhibit suppressed polarization growth (Fig. S4e), indicative of reduced impedance rise. Furthermore, the coulombic efficiency (Fig. S4f) approaches 100% for the TTE-containing cells, demonstrating that anion-rich solvation promotes stable Li plating/stripping and minimizes parasitic reactions.

To analyze the kinetic behavior, we performed Arrhenius fitting of the temperature-dependent impedance data. Impedance measurements were carried out from 30 °C to −10 °C to study the interfacial kinetics of the electrolytes. As the temperature decreases, the overall resistance increases and the spectra change from two overlapping semicircles at higher temperatures to three clearly separated semicircles at lower temperatures. The contact and interfacial resistances are difficult to distinguish at higher temperatures because they have similar characteristic frequencies. However, these processes become easier to separate at lower temperatures.[15]

The Nyquist plots (Fig. S5) were analyzed using an equivalent circuit model (Fig. S5(f)) composed of an ohmic resistance corresponding to the electronic and ionic solution resistance (R_s), three R–CPE elements representing contact resistance, interfacial resistance, and charge-transfer resistance, together with a Warburg diffusion element.[15,24] The temperature dependence of the impedance follows an Arrhenius equation (eqn (1)), indicating that the resistance increases as the temperature decreases. Activation energies for the individual resistance components were obtained from the Arrhenius plots and are summarized in Fig. S6.

The activation energy of the R_S increases as the TTE content increases. This is consistent with the higher viscosity of the TTE-containing electrolytes, which slows Li^+ movement in the bulk electrolyte. This trend agrees with the Li^+ diffusivity obtained from ^7Li NMR measurements and the viscosity results. In contrast, the activation energy of interfacial resistance (R_{SEI}) decreases as the TTE content increases. According to the ^7Li and ^{19}F NMR results, introducing TTE alters the Li^+ solvation

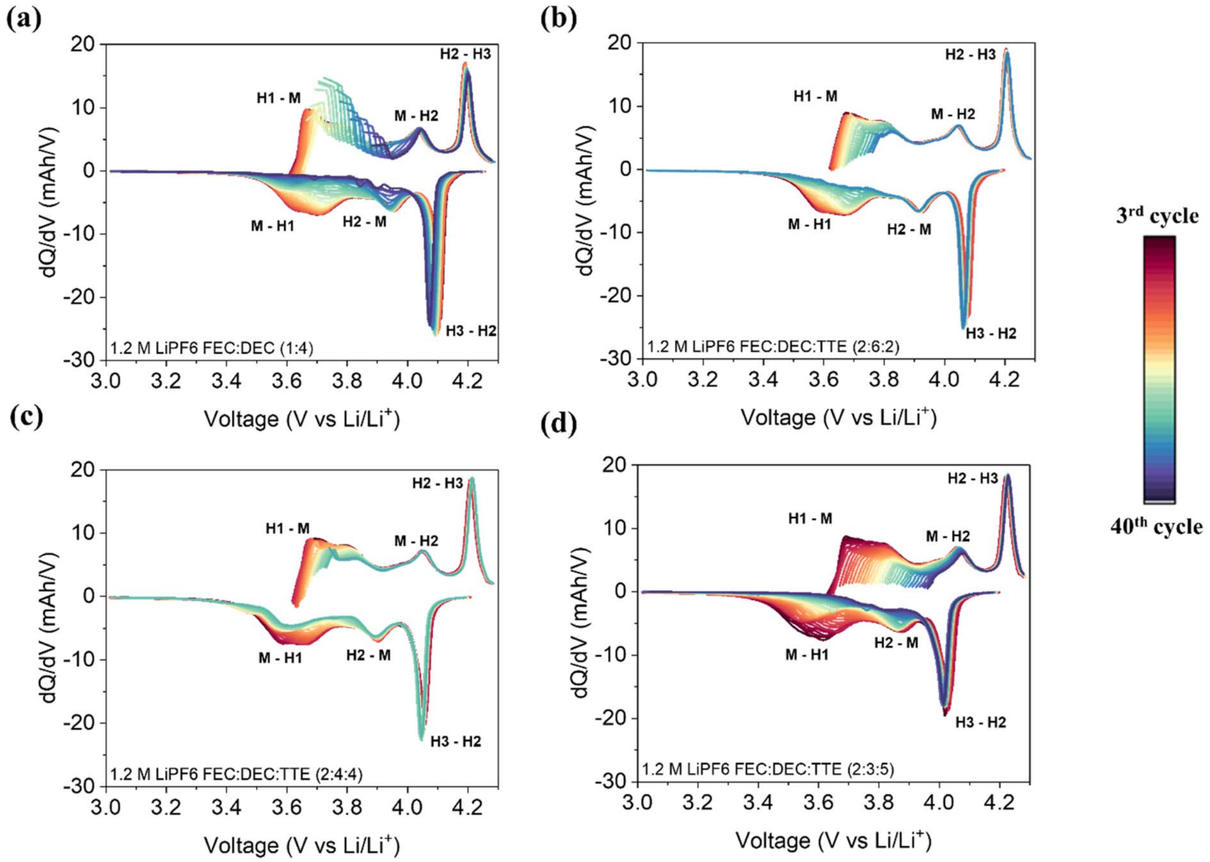

Fig. 3 dQ/dV plots during cycling performance of anode-free NMC90 + Li_2NiO_2 in coin-cells with varying FEC : DEC : TTE electrolyte formulations. (a) 1.2 M $LiPF_6$ in FEC : DEC (1 : 4) (b) 1.2 M $LiPF_6$ in FEC : DEC : TTE (2 : 6 : 2) (c), 1.2 M $LiPF_6$ in FEC : DEC : TTE (2 : 4:4), and (d) 1.2 M $LiPF_6$ in FEC : DEC : TTE (2 : 3 : 5).

structure in the carbonate-based electrolyte. Because TTE has weak solvating ability, more anions participate in the Li^+ solvation sheath, resulting in increased formation of contact ion pairs and ion aggregates. These anion-containing structures are more likely to be reduced at the electrode surface, leading to increased LiF formation.[25] XPS analysis is presented in a later section to examine this hypothesis. The resulting SEI layer is likely more stable and thinner, which may help Li^+ move through the interphase more easily and lower the activation energy.[26] In contrast, the activation energy of the charge-transfer resistance increases as the TTE content increases. The stronger ion pairing and aggregated solvation structures can increase the energy barrier associated with Li^+ desolvation at the electrode interface, leading to a higher activation energy for the charge-transfer process. As a result, the activation energy associated with the overall impedance shows only minor different among the electrolytes. Overall, these results suggest that TTE affects different resistance components in different ways. It slightly increases the resistance related to Li^+ movement in the bulk electrolyte, lowers the barrier for Li^+ transport through the SEI, and increases the activation energy of the charge-transfer step.

To evaluate impedance growth after cycling, EIS was performed to probe the interfacial evolution of the cells before and after cycling at 30 °C. The impedance spectra (Fig. S7) were analysed using an equivalent circuit model, as shown in Fig. S5(f), and the fitted parameters are summarized in Tables S3 and S4. As shown in the Nyquist plots (Fig. S7), the electrolyte without TTE exhibits significant impedance growth after cycling. In contrast, all electrolytes containing TTE show much smaller impedance increases compared to the control electrolyte.

This observation is consistent with the dQ/dV evolution during coin-cell cycling. Cells without TTE display pronounced resistance growth upon cycling, which is mainly attributed to poor coulombic efficiency caused by non-uniform lithium deposition and continuous dead-lithium accumulation. In contrast, the incorporation of TTE suppresses impedance growth by stabilizing lithium deposition and improving coulombic efficiency, thereby reducing dead-lithium formation. The underlying mechanism will be further discussed in the following section.

3.4 Electrochemical performance in Li/Cu half cell

To directly assess the influence of electrolyte composition on lithium plating and stripping behavior, Li‖Cu half cells with varying TTE contents were investigated. As shown in Fig. S8a, all electrolytes exhibit comparable overpotentials during the first lithium plating on the Cu foil, indicating that variations in the FEC : DEC : TTE ratio do not significantly affect the initial lithium nucleation barrier. Fig. S8b presents the lithium plating–stripping voltage profiles recorded at an areal capacity of 2 mA h cm^{-2}. For the TTE-free electrolyte (0% TTE), a pronounced voltage dip appears at the onset of each lithium plating step. This recurring nucleation-related voltage dip indicates repeated fresh lithium nucleation in every cycle,[27] which is commonly associated with non-uniform lithium deposition, repeated SEI rupture, and continuous dead-lithium formation, ultimately leading to poor coulombic efficiency. Electrolytes containing low TTE contents (0–20 vol%) exhibit similar voltage profiles and polarization behavior, suggesting that limited TTE incorporation does not substantially alter lithium deposition characteristics. In contrast, electrolytes with higher TTE contents (30–50 vol%) display a markedly reduced nucleation-related voltage dip after the first cycle. This behavior indicates a transition from repeated lithium re-nucleation to more uniform and continuous lithium growth. Such improvement is attributed to the formation of a LiF-rich inner SEI in TTE-containing electrolytes. This LiF-dominated interphase provides a mechanically robust and chemically stable interface that promotes homogeneous lithium deposition on the Cu surface, thereby enhancing the reversibility of lithium plating and stripping. Consistently, the coulombic efficiency data (Fig. S8c) show a systematic increase with increasing TTE content, further confirming improved lithium reversibility. Additional insight is provided by Fig. S9, which compares lithium plating–stripping voltage profiles in the 2nd and 60th cycles. In the early cycles, all electrolytes exhibit an initial nucleation peak followed by a secondary voltage plateau, which is commonly associated with the formation of high-surface-area lithium (HSAL, often referred to as dendritic lithium) and is indicative of low plating–stripping efficiency.[28] With increasing TTE content, this secondary plateau becomes progressively less pronounced. After extended cycling (the 60th cycle), electrolytes with low TTE content continue to show distinct nucleation peaks and HSAL-related features, evidencing repeated lithium re-nucleation, poor coulombic efficiency, and ongoing lithium inventory loss driven by continuous SEI growth and electrolyte decomposition. By contrast, electrolytes containing higher TTE contents (≥30 vol%) exhibit a substantially suppressed secondary plateau, which nearly disappears in the 50 vol% TTE electrolyte. This evolution signifies more uniform lithium deposition, reduced HSAL formation, and improved interfacial stability in TTE-rich electrolytes, consistent with their superior coulombic efficiency and cycling stability.

To evaluate oxidative stability, linear sweep voltammetry (LSV) and high voltage chronoamperometry measurements were performed (Fig. S10 and S11). As shown in Fig. S10, the baseline electrolyte (1.2 M $LiPF_6$ in FEC : DEC = 1 : 4, without TTE) exhibits an oxidation onset at approximately 4.3 V. In contrast, electrolytes containing TTE show a delayed onset, suggesting improved oxidative stability. In addition, chronoamperometry measurements (Fig. S11) show that electrolytes with higher TTE content exhibit lower residual current during high voltage holds, indicating suppressed parasitic reactions and improved interfacial stability.

3.5 Scaled-up performance in 18650 anode-free cylindrical cells

Building on the coin-cell results, the electrolyte formulations were scaled up and evaluated in commercially relevant anode-free NMC90 + Li_2NiO_2 18650 cylindrical cells. In this stage, the electrolyte composition was further expanded to include 10 and 30 vol% TTE, enabling a systematic assessment across the full 0–50 vol% TTE range. Fig. 4 summarizes the electrochemical performance of anode-free 18650 cells employing six electrolyte formulations with varying TTE contents. The initial charge–discharge profiles (Fig. 4a) show that the baseline electrolyte (0 vol% TTE, black curve) delivers the highest initial coulombic efficiency (ICE) of approximately 74.6%, while increasing TTE content leads to a gradual decrease in ICE. As summarized in Fig. 4b, the average ICE values for electrolytes containing 0, 10, 20, 30, 40, and 50 vol% TTE are 74.6%, 70.2%, 68.2%, 66.7%, 62.4%, and 62.2%, respectively. Correspondingly, the average initial specific capacities decrease from 212.4 to 201.0, 200.1, 196.8, 195.8, and 182.7 mA h g^{-1} with increasing TTE content, as shown in Fig. 4c. The reduced ICE observed for TTE-rich electrolytes is attributed to enhanced lithium surface area during the initial plating process. SEM analysis (Fig. S12) reveals that higher TTE contents lead to the formation of finer lithium filaments with smaller grain sizes, resulting in an increased effective surface area. This enlarged surface area accelerates SEI formation during the first cycle, thereby consuming a greater fraction of the limited lithium inventory inherent to anode-free cells and leading to lower initial capacity. This behavior likely originates from the higher viscosity and reduced Li^+ diffusivity of TTE-rich electrolytes, which shorten the Sand's time and promote diffusion-limited lithium deposition.[29]

Despite these differences in initial efficiency, all electrolyte formulations produce predominantly columnar lithium morphologies during first plating. Such morphologies are generally associated with relatively high coulombic efficiency and mechanically coherent lithium growth,[30] indicating that the observed ICE penalty in TTE-rich electrolytes arises primarily from increased interfacial area rather than fundamentally unstable lithium deposition.

Cycling stability results reveal a clear trade-off among capacity retention, polarization (ΔV), specific capacity, and coulombic efficiency. Electrolytes with higher TTE contents exhibit increased polarization throughout cycling, consistent with their higher viscosity and reduced Li^+ transport efficiency.

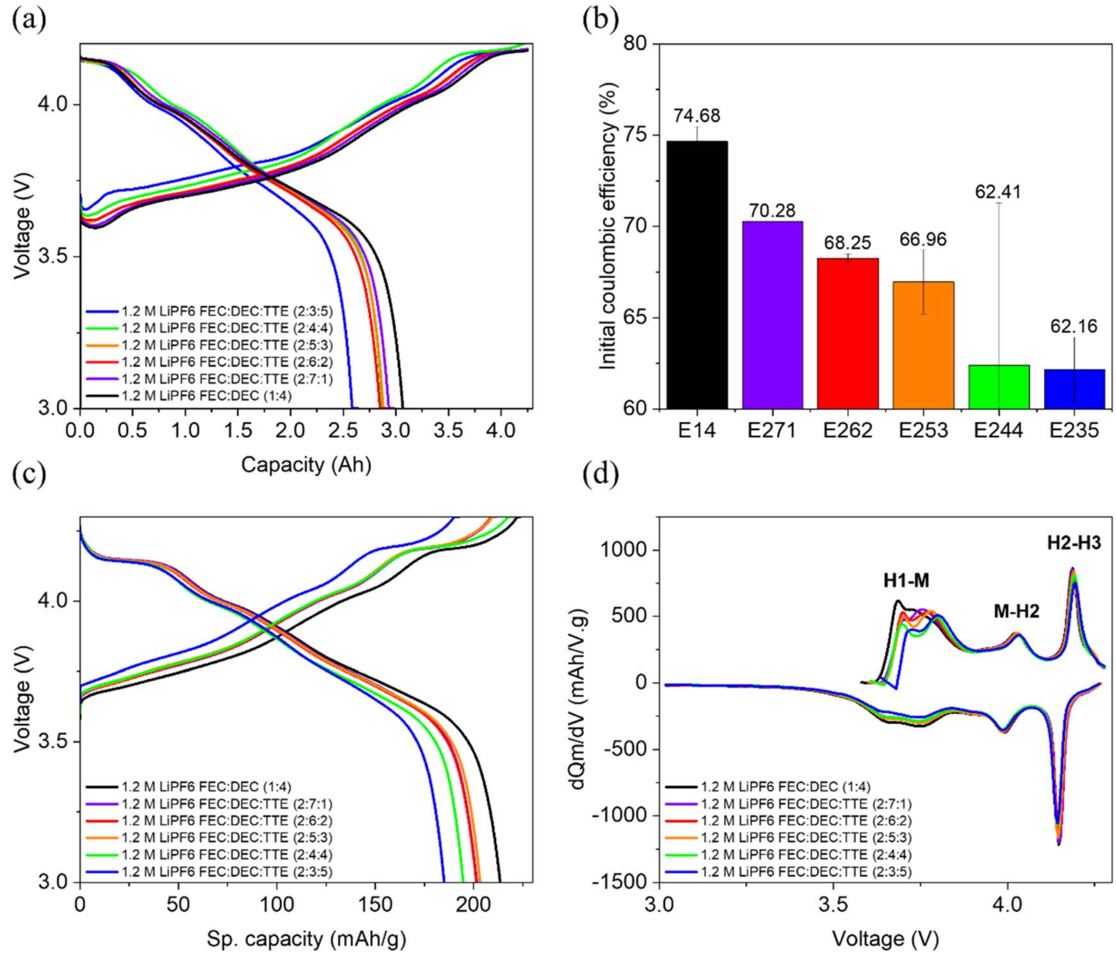

Fig. 4 Electrochemical performance of large-format anode-free NMC90 + Li_2NiO_2 18650 cylindrical cells using electrolytes with varying FEC:DEC:TTE ratios. (a) First cycle charge–discharge voltage profiles. (b) Average initial coulombic efficiency (c) specific capacity of 2nd cycle charge–discharge voltage profiles and (d) differential capacity (d*Q*/d*V*) plot of 2nd cycle. The electrolytes shown are 1.2 M $LiPF_6$ in FEC : DEC (1 : 4) (black), 1.2 M $LiPF_6$ in FEC : DEC : TTE (2 : 7 : 1) (purple), 1.2 M $LiPF_6$ in FEC : DEC : TTE (2 : 6 : 2) (red), 1.2 M $LiPF_6$ in FEC : DEC : TTE (2 : 5 : 3) (orange), 1.2 M $LiPF_6$ in FEC : DEC : TTE (2 : 4 : 4) (green), and 1.2 M $LiPF_6$ in FEC : DEC : TTE (2 : 3 : 5) (blue).

This kinetic limitation lowers the deliverable specific capacity, particularly under the relatively high current densities employed in capacity-retention tests. Despite the increased polarization and reduced capacity, cells containing higher TTE fractions maintain more stable coulombic efficiency during cycling. Consistently, Li||Cu half-cell measurements (Fig. S8c) demonstrate that electrolytes with higher TTE contents deliver higher coulombic efficiency, indicating more uniform lithium deposition and effective suppression of parasitic side reactions.

Notably, all cells exhibit an apparent increase in capacity retention during the initial cycling period. This behavior primarily originates from jelly-roll volume expansion induced by lithium plating, which increases internal pressure within the cylindrical 18650 cell. The resulting compressive stress improves current-collector–electrode contact and promotes more uniform lithium deposition,[23] leading to reduced polarization (lower ΔV) and an apparent enhancement in capacity retention during the early cycles. This mechanically assisted stabilization effect is observed across all electrolyte formulations.

Cells containing 0–10 vol% TTE experience a rapid decline in capacity retention, falling below 80% after approximately 30 cycles. This abrupt failure coincides with a sharp increase in ΔV, indicating severe polarization growth. In contrast, cells containing 20–30 vol% TTE show moderately improved capacity retention, while electrolytes with 40 vol% TTE provide the most favorable balance—significantly enhancing capacity retention with only a modest sacrifice in cell capacity. These trends are consistent with Li||Cu half-cell results. Electrolytes with low TTE content exhibit pronounced voltage plateaus associated with HSAL formation and repeated lithium re-nucleation. Such behavior accelerates electrolyte decomposition and lithium inventory loss, ultimately leading to premature capacity fade. By contrast, Li||Cu measurements demonstrate that increasing TTE content markedly improves lithium deposition behavior on the Cu foil, suppressing HSAL formation and stabilizing the lithium interface. At 50 vol% TTE, although capacity retention is further improved, the overall cell capacity decreases substantially due to low initial coulombic efficiency and an approximately threefold increase in electrolyte viscosity, rendering such formulations impractical for high-loading electrodes (>23 mg cm^{-2}).

Cross-sectional SEM analysis was performed to examine lithium deposition evolution and dead-lithium accumulation before and after cycling (Fig. S13). After the first plating cycle, lithium is uniformly deposited on the Cu foil, forming layers with thicknesses of approximately 15.5, 17.0, and 20.5 μm for electrolytes containing 0%, 20%, and 50% TTE, respectively. After 20 plating cycles, the apparent lithium layer thickness increases to approximately 21, 21, and 24 μm for the same electrolyte compositions. Importantly, the incremental thickness growth in the 50 vol% TTE electrolyte is substantially smaller than that observed in the TTE-free system, indicating suppressed accumulation of electrochemically inactive ("dead") lithium during repeated plating–stripping. This more controlled lithium thickness evolution reflects improved deposition reversibility in TTE-rich electrolytes, in agreement with both full-cell and Li||Cu electrochemical results. The enhanced performance is attributed to the formation of a LiF-rich inner SEI layer in TTE-containing electrolytes, the composition and chemical characteristics of which are discussed in detail in the following section.

Overall, these results identify the electrolyte containing 40 vol% TTE (FEC : DEC : TTE = 2 : 4 : 4, v/v/v) as the optimal formulation. This composition achieves the best balance between high initial capacity (≈190 mA h g^{-1}), moderate polarization, stable coulombic efficiency, enhanced cycling stability, and intrinsic safety, while avoiding the severe kinetic penalties and capacity loss associated with excessively high TTE contents (Fig. 5).

3.6 Interphase composition and depth-resolved SEI chemistry

The superior electrochemical stability of the TTE-containing electrolytes originates from the formation of a chemically and mechanically robust SEI. To elucidate the interfacial chemistry, XPS combined with depth profiling was performed on the lithium metal surface after cycling. As shown in Fig. 6, the SEI exhibits a stratified chemical structure that evolves systematically with electrolyte composition.

Depth-resolved XPS analysis reveals the evolution of the SEI composition formed in electrolytes with different FEC : DEC : TTE ratios at sputtering time of 0, 20, and 60 s under Ar$^+$ sputtering at an accelerating voltage of 500 V. The sputtering rate was calibrated using a SiO_2 reference standard, yielding an average rate of approximately 30 nm min^{-1}. Based on this calibration, sputtering times of 20 and 60 s correspond to nominal depths of approximately ∼10 and ∼30 nm, respectively. At the outermost surface (0 nm), the SEI in all electrolytes consists of a mixture of inorganic species and organic components derived from the reductive decomposition of FEC, DEC, and PF_6^-. The relative atomic percentages are similar across all electrolytes as shown in Fig. S14.

Clear differences appear at greater sputtering depths. At 10 and 30 nm, the relative fraction of carbon-rich organic species decreases, while the contribution of inorganic components increases, as reflected by the higher Li 1 s signal intensity. This trend suggests gradual enrichment of inorganic phases in the inner SEI due to the partial dissolution or transformation of organic components during SEI evolution. Overall, the SEI compositions are similar across the different electrolyte formulations. Notably, the P 2p atomic percentage increases with increasing TTE content, indicating a greater contribution from PF_6^- reductive decomposition in electrolytes containing higher TTE concentrations.

However, a noticeable difference is observed in the deconvoluted Li 1s spectra. As shown in Fig. S15, the deconvolution of the Li 1s spectra provides further insight into the depth-dependent inorganic composition of the SEI. As shown in Fig. 6a–c, the deconvoluted Li 1s spectra indicate the presence of inorganic SEI components, including LiF, Li_2CO_3, and Li_2O. In the electrolyte without TTE, LiF is the dominant species at the outermost surface. This observation is consistent with the preferential reductive decomposition of FEC, where ring–

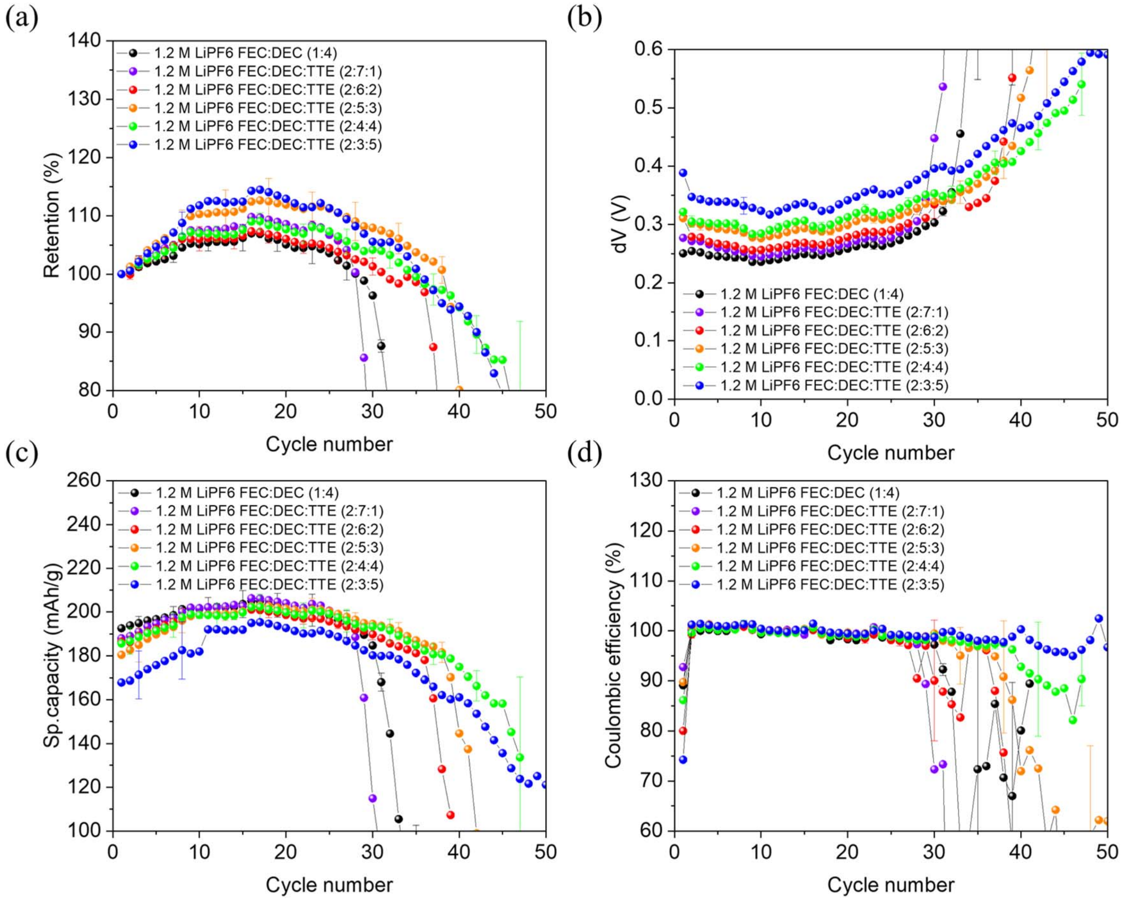

Fig. 5 Cycling performance of large-format anode-free NMC90 + Li_2NiO_2 18650 cylindrical cells using electrolytes with varying FEC : DEC : TTE ratios. (a) Capacity retention, (b) polarization growth (d*V*), (c) specific capacity retention, (d) coulombic efficiency, and during long-term cycling in the 3.0–4.3 V range (100% SOC). The electrolytes shown are 1.2 M $LiPF_6$ in FEC : DEC (1 : 4) (black), 1.2 M $LiPF_6$ in FEC : DEC : TTE (2 : 7 : 1) (purple), 1.2 M $LiPF_6$ in FEC : DEC : TTE (2 : 6 : 2) (red), 1.2 M $LiPF_6$ in FEC : DEC : TTE (2 : 5 : 3) (orange), 1.2 M $LiPF_6$ in FEC : DEC : TTE (2 : 4 : 4) (green), and 1.2 M $LiPF_6$ in FEC : DEC : TTE (2 : 3 : 5) (blue).

opening reactions generate LiF accompanied by CO_2 evolution. Moreover, the generated CO_2 can subsequently contribute to Li_2CO_3 formation through secondary reactions with Li_2O or through further conversion of FEC-derived intermediates.[31,32] However, at a sputtering depth of ∼30 nm, Li_2O becomes the dominant inorganic species, suggesting that the inner SEI is enriched with solvent-derived decomposition products.[32,33]

In the electrolyte containing 20 vol% TTE, solvation restructuring, as confirmed by ^{7}Li and ^{19}F NMR, shifts the coordination environment toward increased Li^+–PF_6^- contact ion pairing and aggregate formation.[16,19] Under this condition, FEC molecules participate more strongly in the primary Li^+ solvation sheath, which increases their likelihood of reduction at the electrode interface. This enhanced reduction is supported by the increased CO_2 evolution detected by DEMS, as discussed in the next section. The higher CO_2 generation correlates with an increased Li_2CO_3 content at the outer SEI surface At sputtering depths of 10 and 30 nm, the relative atomic percentage of LiF is significantly higher than that in the TTE-free electrolyte, indicating enhanced salt-derived SEI formation.[34–37] Nevertheless, the inner SEI contains LiF, Li_2O, and Li_2CO_3 in comparable proportions. This observation suggests that both solvent-derived (FEC) and anion-derived (PF_6^-) reduction pathways contribute to the overall SEI formation.

When the TTE content increases to 50 vol%, LiF becomes the dominant inorganic species at all across sputtering depths, while the Li_2CO_3 content decreases. This observation correlates with the DEMS results, which show reduced CO_2 evolution, indicating that FEC mainly exists as a free solvent with a lower reduction potential. This trend is consistent with the NMR results, which indicate extensive Li^+–PF_6^- contact ion pairing and aggregate formation. Under these conditions, PF_6^- increasingly replaces FEC in the Li^+ solvation sheath and promotes PF_6^- reductive decomposition. At the same time, the P 2p atomic percentage increases with increasing TTE content, further supporting the dominant contribution of salt-derived species to inner SEI formation. Overall, these depth-resolved XPS results demonstrate that TTE-induced solvation restructuring shifts the dominant reduction pathway from solvent-driven to anion–driven processes, which governs the chemical composition and layered structure of the SEI.

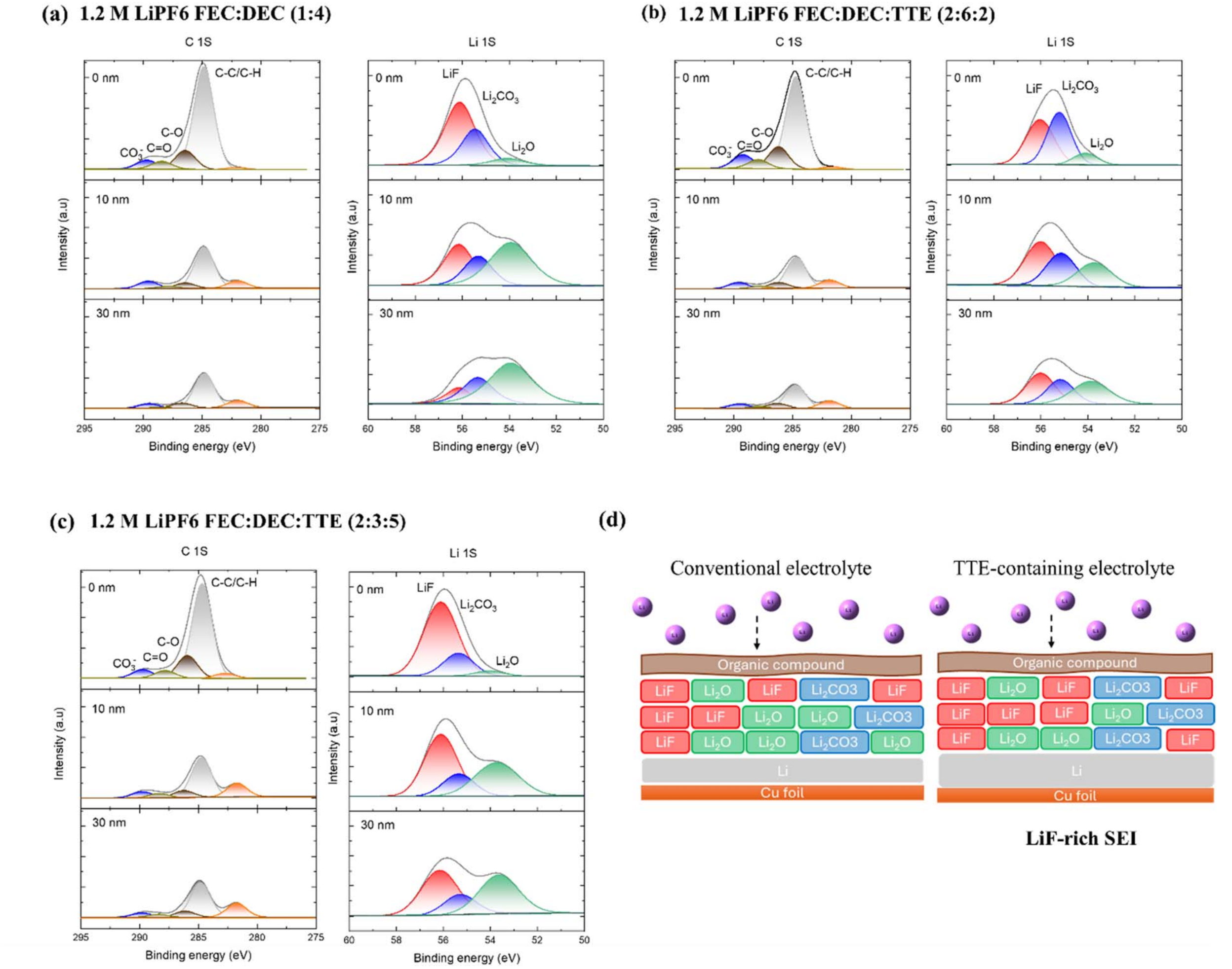

Fig. 6 Depth-resolved XPS analysis of the SEI formed on the anode of anode-free NMC90 + Li_2NiO_2 cells with varying electrolyte formulations. (a) 1.2 M $LiPF_6$ in FEC : DEC (1 : 4), (b) 1.2 M $LiPF_6$ in FEC : DEC : TTE (2 : 6 : 2), (c) 1.2 M $LiPF_6$ in FEC : DEC : TTE (2 : 3 : 5) and (d) schematic illustration comparing the SEI structure formed in conventional carbonate electrolyte and TTE-containing electrolyte, highlighting the formation of a LiF-rich and more inorganic SEI in the presence of TTE.

Deconvoluted C 1s and Li 1s spectra are shown at sputtering depths of 0, 20, and 50 nm (Fig. 6c). The C 1s spectra reveal progressive suppression of organic carbonate species and enrichment of C–C/C–H bonds with increasing TTE content, indicating reduced solvent decomposition. The Li 1s spectra show an increasing contribution of inorganic LiF and Li_2O components relative to Li_2CO_3 in TTE-containing electrolytes (as shown in Fig. 6d), confirming the formation of an inorganic, LiF-rich SEI. This compositional evolution evidences that the fluorinated ether diluent promotes anion-derived reduction pathways and stabilizes the interphase structure by favoring the preferential decomposition of PF_6^- rather than organic carbonates.

3.7 Gas evolution mechanisms during cycling

To elucidate the decomposition pathways of the electrolytes during cycling, DEMS was employed to monitor the evolution of gaseous products in real time. As shown in Fig. 7, the principal gaseous species detected were carbon dioxide (CO_2), hydrogen (H_2), and ethane (C_2H_6). Gas evolution predominantly occurred during the charging process above 4.1 V and during subsequent discharge, indicating contributions from both oxidative and reductive electrolyte decomposition. Among these products, C_2H_6 originates from the reductive fragmentation of the DEC solvent.[38] The formation of CO_2 is more complex, arising from multiple pathways: at moderate potentials (~4.2 V), FEC undergoes reductive decomposition to yield CO_2 while simultaneously forming LiF, Li_2O and Li_2CO_3, the principal inorganic components of the SEI.[31] At higher potentials (>4.4 V), additional CO_2 evolution is attributed to oxidative electrolyte degradation triggered by reactive singlet oxygen released from the Ni-rich cathode surface.[39]

The incorporation of TTE substantially alters the gas evolution behavior through its effect on solvation structure. NMR analysis in Fig. 2a and b above confirms that increasing TTE concentration displaces the weakly coordinating FEC and DEC molecules from the primary Li^+ solvation sheath, allowing PF_6^- anions to associate more with Li^+, leading to the formation of contact ion pairs (CIPs) and aggregation (AGG).[40]

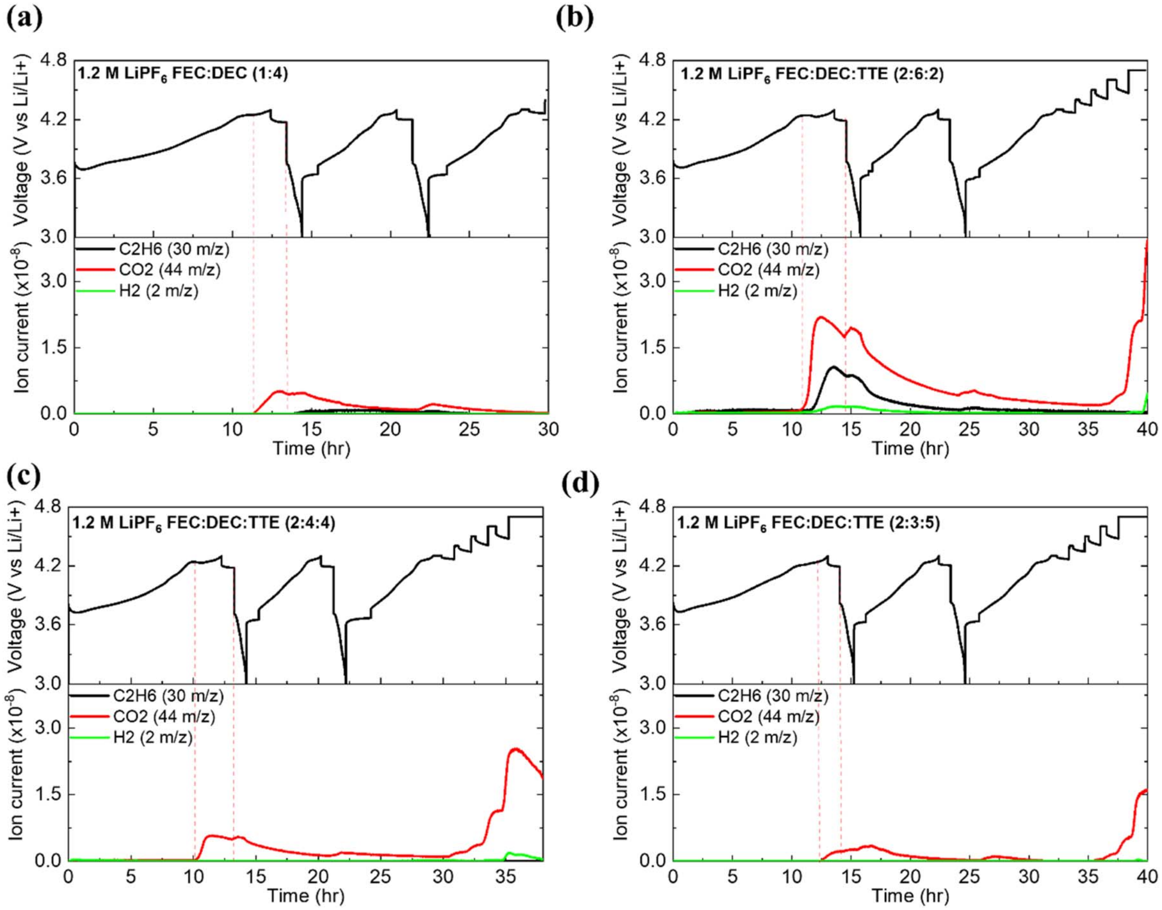

Fig. 7 Differential electrochemical mass spectrometry (DEMS) analysis of gaseous products during initial cycling and high-voltage region of varying FEC : DEC : TTE electrolyte formulations. The figure displays DEMS current signals for gaseous species generated during the electrochemical cycling of different electrolyte formulations (a) 1.2 M $LiPF_6$ in FEC : DEC (1 : 4), (b) 1.2 M $LiPF_6$ in FEC : DEC : TTE (2 : 6 : 2), (c) 1.2 M $LiPF_6$ in FEC : DEC : TTE (2 : 4 : 4), and (d) 1.2 M $LiPF_6$ in FEC : DEC : TTE (2 : 3 : 5). The color coding for the gaseous species is as follows: black represents ethane (C_2H_6), red represents carbon dioxide (CO_2), and green represents hydrogen (H_2).

This rearrangement may alter the reduction behaviour of electrolyte species at the anode surface. Based on our hypothesis, at low TTE content (20 vol%), the CIP and AGG solvation structures may not yet be fully established. As a result, carbonate-based solvents (FEC and DEC) are more involved in the solvation sheath and can undergo reductive decomposition more readily, which is consistent with the increased gas evolution observed in Fig. 7b. In contrast, at higher TTE concentrations (≥40 vol%), the solvation structure is hypothesized to shift toward CIP- and AGG-dominated configurations. Such a solvation environment may influence the reduction pathway of FEC, resulting in less CO_2 generation, as shown in Fig. 7c and d.

Importantly, the DEMS gas-evolution trends correlate directly with the XPS-derived SEI compositions (Fig. 6). Electrolytes with low TTE content exhibit pronounced CO_2 evolution during formation and high-voltage charging, consistent with the higher Li_2CO_3 compound identified by XPS and indicative of ongoing carbonate-based solvent decomposition. Conversely, electrolytes containing higher TTE fractions (40–50 vol%) show strongly suppressed CO_2 evolution, in agreement with the reduced Li_2CO_3 contribution and dominant LiF signal observed in the corresponding XPS depth profiles. The convergence of DEMS and XPS results thus provide independent and complementary evidence that TTE-induced anion-dominated solvation suppresses solvent-derived SEI formation and gas generation, while promoting the rapid formation LiF-rich interphase.

Overall, these observations demonstrate that electrolyte decomposition and gas evolution are strongly governed by solvation sheath. The transition from a solvent-dominated to an anion-dominated coordination environment stabilizes the electrolyte against both reductive and oxidative decomposition. This mechanistic understanding further corroborates the NMR, XPS and DEMS findings, establishing that the fluorinated ether diluent not only mitigates flammability but also governs interfacial reactivity through the control of the Li^+ solvation structure.

3.8 Chemical decomposition pathways of cycled electrolytes

The chemical stability of the electrolytes after 20 cycles was examined using ^1H-NMR and GC-MS (Fig. S16–S17, Tables S8), revealing decomposition pathways that depend strongly on the solvation sheath created by TTE. For the control electrolyte (1.2 M $LiPF_6$ in FEC : DEC (1 : 4)), the ^{1}H-NMR spectra show clear signatures of vinylene carbonate (VC, $\delta = 7.02$ ppm), a characteristic reductive decomposition product of FEC, along with HF from $LiPF_6$ hydrolysis and resonances corresponding to lithium ethyl carbonate (LEC) and acetate-type species originating from DEC fragmentation.[31,41–43] These species suggest that both carbonate solvents including DEC and FEC undergo concurrent reductive decomposition, producing a heterogeneous organic–inorganic SEI and gaseous by-products (CO_2, C_2H_6), consistent with DEMS observations.

In contrast, the disappearance of VC and the appearance of formic acid suggest a change in the dominant decomposition processes. This observation indicates that the reductive decomposition of FEC and DEC is reduced under these conditions. However, the presence of formic acid suggests that oxidative decomposition of DEC still occur, as formic acid is commonly associated with the oxidation of linear carbonate solvents.[44] As the solvation sheath shifts toward CIP andAGG configurations, carbonate solvents, especially DEC, may become more susceptible to oxidative reactions.

However, oxidative stability tests using linear sweep voltammetry (LSV) and chronoamperometry show that increasing TTE content improves the overall oxidative stability of the electrolyte. Therefore, the small trace of oxidative decomposition products from DEC is unlikely to significantly affect overall cell performance. A more detailed investigation of this mechanism will be addressed in future work.

3.9 Mechanical stress and accumulation-macroscopic structural failure

The microscale stabilization of lithium deposition enabled by TTE-containing electrolytes translates directly into macroscopic mechanical behavior at the cell level in 18650-format anode-free batteries. As shown in Fig. 8, cells employing the TTE-free electrolyte (0% TTE) exhibit pronounced radial jelly-roll expansion after cycling, accompanied by severe casing deformation and current-collector distortion (Fig. 8a). This excessive expansion originates from rapid lithium accumulation and extensive dead-lithium formation, which substantially increase the effective lithium thickness and generate high internal stress within the rigidly confined cylindrical architecture. Once the mechanical tolerance of the steel casing is exceeded, electrical contact degradation and structural distortion occur, ultimately leading to catastrophic cell failure.

In contrast, cells containing TTE display markedly reduced jelly-roll expansion, with the extent of expansion decreasing systematically as the TTE content increases. The measured jelly-roll diameters after cycling (Fig. 8b–e) are approximately 19.02 mm for 0% TTE, 18.55 mm for 20% TTE, and 17.34–17.55 mm for 40–50% TTE, compared with an inner casing diameter of 18 mm. While cells with 0% and 20% TTE exceed the casing diameter and therefore experience severe mechanical constraint, cells containing 40–50% TTE remain within the elastic tolerance of the steel casing. This reduced radial expansion is consistent with more uniform lithium deposition and suppressed dead-lithium accumulation, as corroborated by Li||Cu electrochemical measurements and cross-sectional SEM analysis.

Although lithium plating remains cumulative in all anode-free configurations, the introduction of TTE clearly slows lithium thickness growth and mitigates volumetric strain, thereby delaying the onset of mechanically induced failure. Notably, cells containing 40–50% TTE nevertheless exhibit an abrupt capacity drop after approximately 50 cycles. This late-stage failure is likely associated with electrolyte depletion in the limited electrolyte reservoir of the 18650 configuration, arising from continuous SEI growth over extended cycling rather than from immediate mechanical instability.

Additional insight is provided by macroscopic post-mortem observations following cell disassembly (Fig. S18). In the TTE-free electrolyte (0% TTE, Fig. S18a–c), the cathode exhibits severe deformation and mechanical damage, indicative of strong shear stresses generated during cycling due to uncontrolled lithium accumulation and radial expansion. Upon introducing 20% TTE (Fig. S18d–f), electrode deformation is noticeably reduced, suggesting partial alleviation of mechanical stress. Further increasing the TTE content to 40% and 50% (Fig. S18g–l) yields substantially improved structural integrity, with minimal cracking or distortion. Notably, severe adhesion between lithium, separator, and anode is observed in all samples, which limits further detailed morphological analysis of the anode–separator interface.

To quantitatively assess the mechanical origin of failure, controlled jelly-roll expansion experiments were conducted (Fig. 9). Five anode-free jelly rolls with initial diameters of 16.0–17.0 mm were charged to 4.3 V, resulting in radial expansion of approximately 0.6 mm for all samples, corresponding to a volumetric strain of ~7.5% (Table S5). For the largest jelly rolls (No. 4 and No. 5), this expansion exceeded the available clearance, causing rupture of the glass containment tube. Using the thin-walled pressure vessel approximation, the internal pressure required to induce fracture was estimated to be ~10.3 MPa, exceeding the yield strength of borosilicate glass. For comparison, an equivalent expansion within a 3A steel 18650 casing would generate an internal pressure of ~8.1 MPa and a radial strain of ~2.8% (Table S7). Although 3A steel possesses a higher yield strength, its thin wall thickness renders it susceptible to plastic deformation under such stresses.

We also tested the cells using a slower charging rate of C/5 and a discharging rate of D/2. The results (Fig. S19) initially exhibit exceptional capacity retention approaching 100%, a result of the high internal pressure imposed by the constrained cylindrical geometry, which promotes compact and uniform Li deposition.[23,45] Interestingly, this stability is transient: beyond ~50 cycles, the cells experience an abrupt capacity collapse. Although a slower charging rate promotes more stable lithium plating, it results in a greater accumulation of deposited lithium on the anode, which causes greater electrode swelling. This catastrophic failure originates from mechanical stresses induced by volumetric expansion during Li plating in the tightly wound jelly roll architecture. Expansion-induced internal pressure causes deformation of the metallic casing, ultimately leading to rupture, as confirmed by the post-mortem images in Fig. S20a–d.

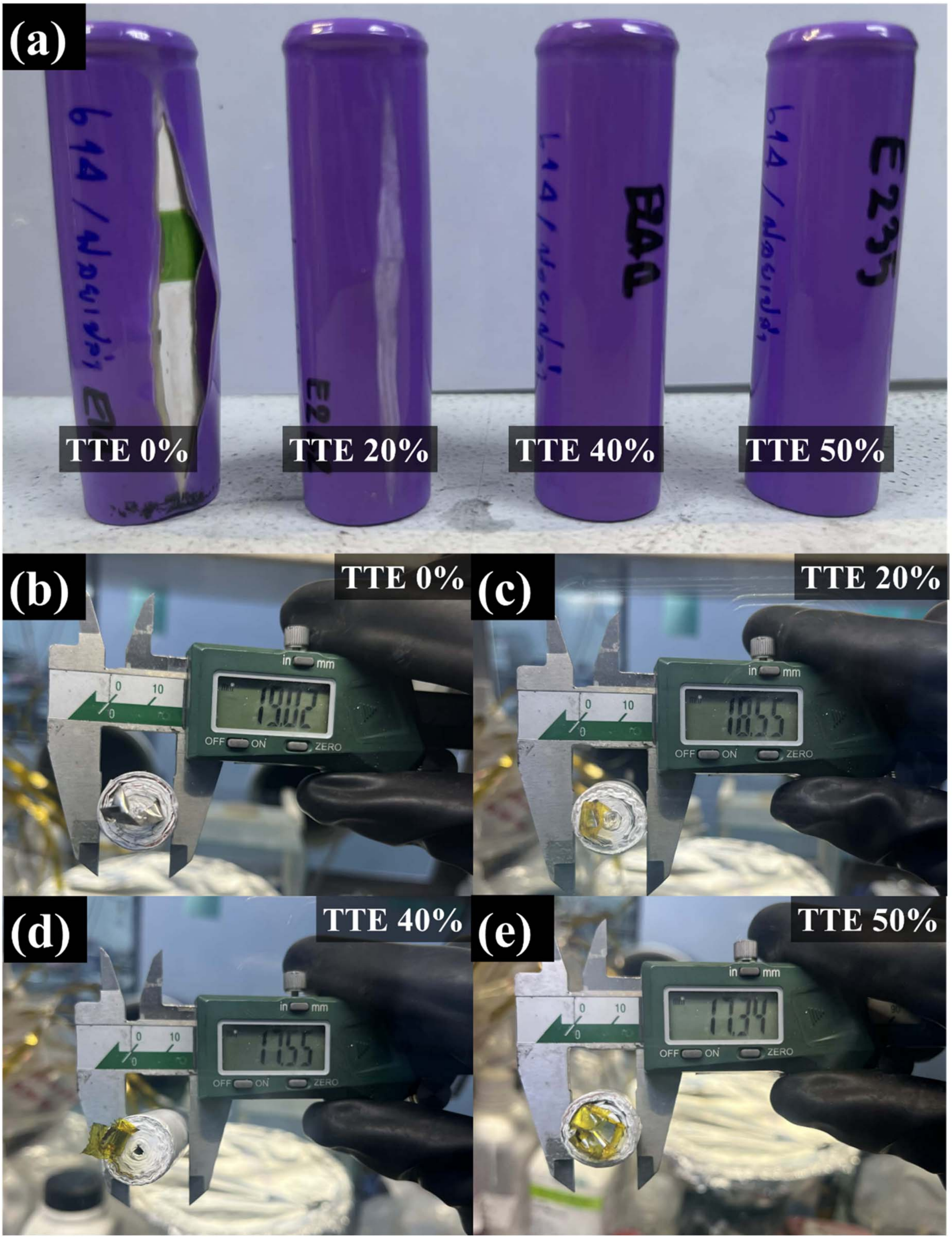

Fig. 8 Post-cycled 18650 anode-free cylindrical cells with electrolytes of varying FEC : DEC : TTE ratios. (a) Photographs of cells after cycling, showing electrolyte-dependent differences in casing deformation. (b–e) Diameter measurements of the disassembled jelly rolls corresponding to electrolytes containing 0%, 20%, 40%, and 50% TTE, respectively.

These results reveal a critical interplay between electrolyte chemistry and mechanical integrity in anode-free cells. Although the mechanical constraints inherent to the anode-free architecture ultimately govern cell failure, the fluorinated ether diluent (TTE) fundamentally stabilizes the electrochemical interface by inducing anion-rich solvation and promoting the formation of a LiF-rich

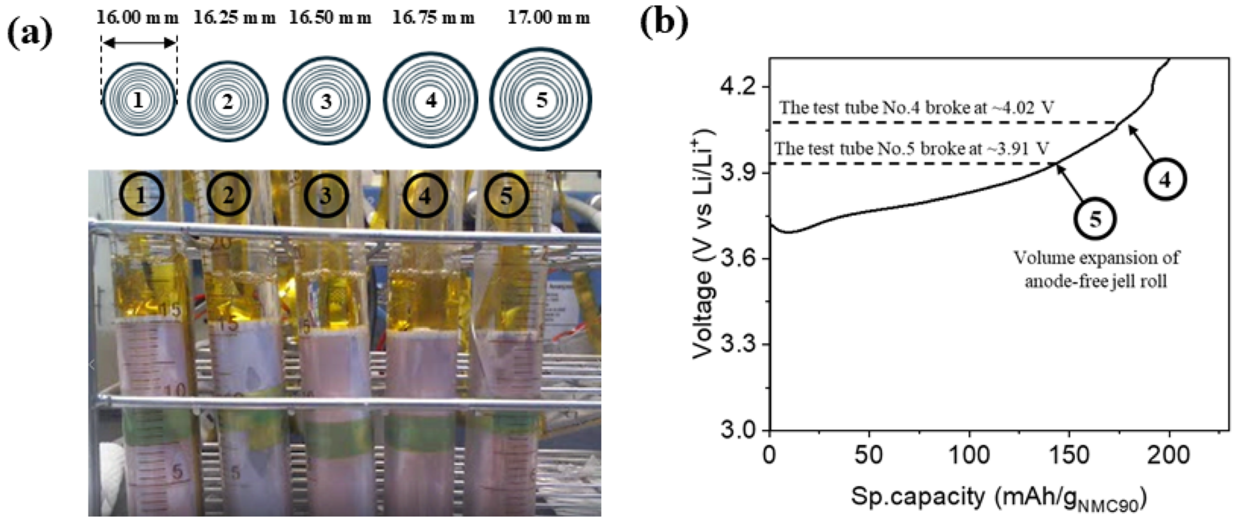

Fig. 9 Jelly roll expansion behavior and electrochemical performance of anode-free jelly rolls. This figure illustrates the relationship between the initial diameter of anode-free jelly rolls and their subsequent expansion during 1st plating. The top left shows the initial diameters (16 mm to 17 mm) of five different jelly rolls (labelled 1–5). (a) The bottom image displays the actual jelly rolls in test tubes, demonstrating their visible cracking of tube Number 5. (b) Charging profile during 1st plating for the anode-free cells. This graph highlights the volume expansion of the anode-free jelly roll during the charge cycle and indicates the voltages at which test tubes #4 and #5 experienced breakage due to this expansion.

SEI. This interphase suppresses dead-lithium accumulation, slows lithium thickness growth, and consequently reduces volumetric expansion in 18650 cells. Together, these insights underscore the necessity of integrated electrochemical–mechanical design strategies that couple solvation engineering with structural accommodation to enable the practical realization of high-energy-density anode-free lithium-metal batteries.

Noted that the identification of mechanically dominant failure is intrinsically linked to the specific geometric and mechanical constraints of the 18650 cylindrical hard-case configuration employed in this study. In this format, lithium plating induces radial expansion of the jelly roll, which is tightly confined by the rigid steel casing. Such confinement converts volumetric expansion directly into hoop stress, leading to rapid stress accumulation at the jelly roll–case interface and ultimately resulting in casing deformation, internal delamination, or abrupt mechanical failure once the critical radial strain is exceeded. In contrast, pouch cells lack rigid radial confinement and can accommodate lithium-induced swelling predominantly through out-of-plane (thickness) expansion of the electrode stack. This greater mechanical compliance allows stresses to be distributed over a larger area, thereby delaying catastrophic failure and reducing the likelihood of sudden rupture. Consequently, while radial expansion serves as the dominant failure-triggering mechanism in hard-case cylindrical cells, pouch cells are more likely to exhibit gradual performance degradation governed by interfacial instability, electrolyte depletion, or lithium inventory loss rather than abrupt, mechanically driven collapse.

3.10 Intrinsic safety evaluation under UN38.3 impact testing

The intrinsic safety of the anode-free 18650 cells under mechanical abuse was evaluated using the UN38.3 impact test conducted at a 50% state of charge (SOC). As shown in Fig. 10, the results clearly demonstrate the fundamental role of the fluorinated ether diluent in mitigating thermal runaway. The control cell employing the conventional electrolyte (1.2 M $LiPF_6$ in FEC : DEC (1 : 4)) underwent a violent exothermic reaction upon impact, rapidly exceeding 90 °C and leading to catastrophic thermal runaway (Fig. 10a). In contrast, all TTE-containing electrolytes exhibited outstanding mechanical and thermal stability—no ignition, gas venting, or temperature rise was observed during testing (Fig. 10b–d).

Thermal runaway in lithium-based batteries is typically initiated by a short-circuit–induced heat spike, followed by a sequence of self-accelerating exothermic reactions. A local internal short generates intense Joule heating, resulting in a highly localized temperature rise at the electrode–electrolyte interface. The earliest chemical response to this perturbation occurs at the SEI, where elevated temperature and potential accelerate parasitic interfacial reactions. Decomposition of unstable SEI components exposes fresh reactive surfaces, producing additional heat and gas. If the rate of heat generation exceeds heat dissipation, positive feedback loops involving reaction kinetics, gas evolution, and separator degradation develop, ultimately leading to thermal runaway. Notably, bulk electrolyte combustion and cathode oxygen release occur only at later stages, after the system has already crossed a critical thermal threshold.[46]

From this mechanistic perspective, the SEI represents the primary control point determining whether a short circuit escalates into thermal runaway. LiF-rich SEIs are particularly effective at suppressing early-stage heat generation because LiF is thermodynamically stable, chemically saturated, and does not decompose or release gaseous products within the temperature range relevant to runaway initiation.[26,33] In contrast, organic SEI components and Li_2CO_3 are metastable

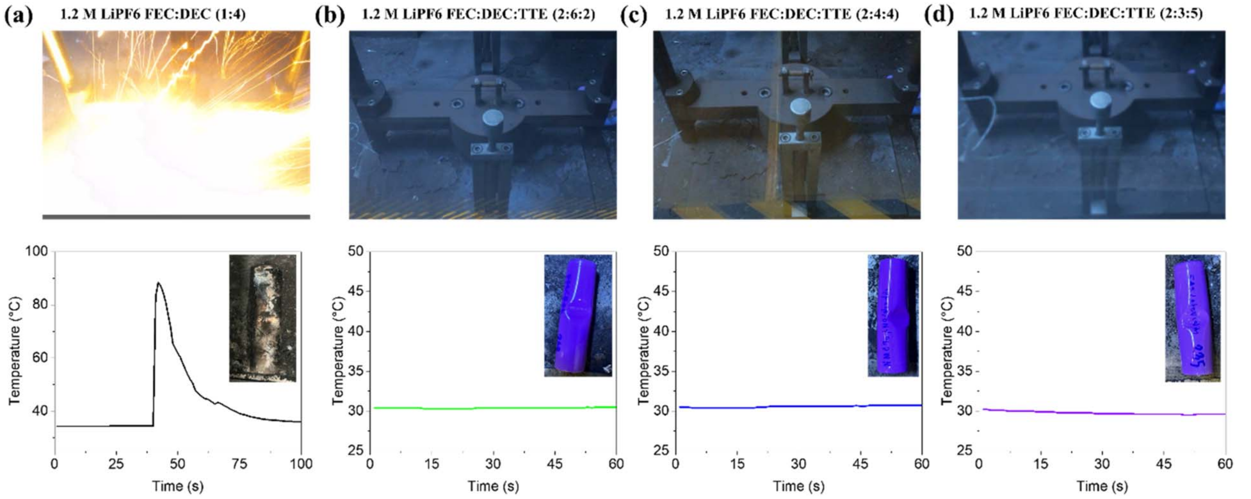

Fig. 10 UN38.3 impact safety test results for anode-free NMC90 + Li_2NiO_2 18650 cylindrical cells using electrolytes with varying FEC : DEC : TTE compositions at 50% state of charge (SOC). (a) 1.2 M $LiPF_6$ in FEC : DEC (1 : 4), (b) 1.2 M $LiPF_6$ in FEC : DEC : TTE (2 : 6 : 2), (c) 1.2 M $LiPF_6$ in FEC : DEC : TTE (2 : 4 : 4), and (d) 1.2 M $LiPF_6$ in FEC : DEC : TTE (2 : 3 : 5). Each panel displays the visual outcome after mechanical impact, the corresponding temperature profile, and an inset image of the post-test cell condition. The conventional electrolyte (a) undergoes violent thermal runaway with an intense exothermic reaction exceeding 90 °C, whereas all TTE-containing formulations (b–d) remain thermally stable without visible ignition or temperature escalation. These results confirm that the fluorinated ether diluent effectively suppresses combustion and ensures non-flammable, impact-tolerant behavior, fulfilling UN38.3 safety criteria for large-format anode-free cells.

and can undergo exothermic decomposition under thermal or electrochemical stress. Owing to its low free-energy state, wide electrochemical stability window, and electronic insulating nature, LiF neither participates in exothermic reactions nor supports electron-driven parasitic processes or radical chain reactions. Consequently, a LiF-rich SEI limits both the magnitude and spatial propagation of interfacial heat generation, thereby reducing the likelihood that localized heating evolves into a self-accelerating thermal runaway event.[26]

The intrinsic non-flammability associated with fluorinated electrolytes and high C–F bond energies plays a complementary but mechanistically later role. High C–F bond dissociation energies reduce the propensity of solvent molecules to undergo radical-driven oxidation and combustion once decomposition or venting occurs. This intrinsic stability primarily influences the severity and propagation of fire after gases are released, rather than the initial onset of thermal runaway inside the cell. Thus, while fluorinated solvents can reduce flame intensity and combustion outside the cell, they do not by themselves prevent the early interfacial reactions that trigger runaway.

Additionally, we have explored the additional formulation which is a dual-salt electrolyte (LiDFOP + $LiBF_4$) that exhibited enhanced safety in pouch cell be passed nail penetration test without catch a fire and explosion. Consistent with the literature, the dual-salt electrolyte demonstrates excellent intrinsic safety characteristics. Our flammability tests confirm that this electrolyte is flammable under open-flame conditions (Fig. S22), yet it remains mechanically safe under UN38.3 impact testing, showing no explosion or thermal runaway (Fig. S21g–i). These results are in agreement with the Dahn group's conclusion that desirable SEI chemistry—rich in inorganic salt-derived species—can effectively suppress violent failure even in the presence of mechanically induced internal shorting.[23] However, despite this favorable safety response, the electrochemical performance of the dual-salt electrolyte is markedly inferior to that of 1.2 M $LiPF_6$ in FEC : DEC when implemented in 18650 cells, as shown in Fig. S21a–f. Specifically, cells using the LiDFOP/$LiBF_4$ electrolyte exhibit lower initial capacity, faster capacity decay, increased polarization growth, and reduced coulombic efficiency relative to the $LiPF_6$-based system. These results highlight a critical distinction between interfacial safety stabilization and practical electrochemical reversibility in large-format cylindrical cells.

Taken together, established literature supports a synergistic hierarchy in battery safety mechanisms, in which SEI chemistry—particularly the formation of LiF-rich interphases—plays the dominant role at the earliest stage by suppressing interfacial heat generation and inhibiting the initiation of chain reactions, while intrinsic electrolyte properties, such as high C–F bond energy, become increasingly important at later stages by limiting flammability and combustion propagation. This distinction is critical for guiding future electrolyte design, as it underscores that effective prevention of thermal runaway relies first on controlling early interfacial reaction kinetics, with intrinsic non-flammability providing an additional, secondary layer of safety once failure progresses beyond the interphase.

4. Conclusion

This work demonstrates how fluorinated ether diluents govern solvation chemistry, interphase formation, electrochemical reversibility, and mechanical reliability in large-format anode-free lithium metal batteries. Incorporation of TTE into a localized high-concentration electrolyte restructures the Li^+

solvation shell into a PF_6^--dominated coordination environment, promoting preferential anion reduction and the formation of a dense, LiF-rich SEI. This interphase suppresses parasitic reactions, reduces dead-lithium accumulation, and stabilizes lithium plating and stripping, leading to improved coulombic efficiency, reduced polarization growth, and enhanced cycling stability in both coin cells and 18650-format cells. Despite this substantial interfacial stabilization, cell failure at the cylindrical–cell scale is ultimately governed by lithium-plating-induced volumetric expansion. Jelly-roll expansion and post-mortem analyses reveal that cumulative lithium deposition generates internal stresses approaching the mechanical limits of steel casings, resulting in abrupt capacity collapse. TTE-containing electrolytes mitigate this process by slowing lithium thickness growth and delaying mechanically driven failure, though they cannot fully eliminate it. In addition, TTE imparts significant intrinsic safety benefits. Cells employing TTE-containing electrolytes exhibit non-flammable behavior and pass UN38.3 impact testing without thermal runaway. This safety enhancement arises from a synergistic mechanism in which a LiF-rich SEI suppresses early-stage interfacial heat generation, while the fluorinated ether reduces flammability at later stages. Overall, these findings establish solvation-driven interphase engineering as a powerful strategy to enable high-efficiency, high-energy, and intrinsically safe anode-free lithium metal batteries, while underscoring the need to integrate electrolyte design with mechanical accommodation strategies to achieve long-term durability at practical cell scales.

Author contributions

Nattanon Joraleechanchai: characterizations, fabrication of 18650 lithium battery cells, investigation, formal analysis, writing – review & editing. Nuttida Matkhaw: investigation, formal analysis, writing – review & editing. Thitiphum Sangsanit: fabrication of 18650 lithium battery cells, investigation, formal analysis, writing – review & editing. Worapol Tejangkura: investigation, formal analysis, writing – review & editing. Montree Sawangphruk: funding acquisition, supervision, investigation, resources, writing – review & editing, conceptualization, formal analysis.

Conflicts of interest

The authors declare no conflict of interest.

Data availability

The data that support the findings of this study are available in the supplementary information (SI) of this article. Supplementary information: detailed cell fabrication parameters, electrolyte formulations, and electrochemical testing protocols. Additional impedance analysis, lithium plating/stripping behavior, SEM, XPS, and NMR results provide mechanistic insights into SEI formation and electrolyte decomposition. Practical validation is further supported by 18650 cell performance, post-mortem analysis, mechanical expansion measurements, and safety testing. See DOI: https://doi.org/10.1039/d6sc00025h.

Acknowledgements

This work was financially supported by the Program Management Unit for National Competitiveness Enhancement (PMU-C) by the Office of National Higher Education Science Research and Innovation Policy Council (NXPO) and IRPC Public Company Limited, Thailand Science Research and Innovation (TSRI) under the Fundamental Fund, and the Energy Policy and Planning Office (EPPO), Ministry of Energy, Thailand. In addition, the Frontier Research Centre (FRC) at VISTEC kindly supported this work.

References

1 P. Albertus, S. Babinec, S. Litzelman and A. Newman, Status and challenges in enabling the lithium metal electrode for high-energy and low-cost rechargeable batteries, *Nat. Energy*, 2018, **3**(1), 16–21, DOI: 10.1038/s41560-017-0047-2.

2 J. Betz, G. Bieker, P. Meister, T. Placke, M. Winter and R. Schmuch, Theoretical versus Practical Energy: A Plea for More Transparency in the Energy Calculation of Different Rechargeable Battery Systems, *Adv. Energy Mater.*, 2019, **9**(6), 1803170, DOI: 10.1002/aenm.201803170.

3 K. Tang, L. Tian, Y. Zhang and Z. J. Xu, Anode-free lithium metal batteries: a promising flexible energy storage system, *J. Mater. Chem. A*, 2024, **12**(27), 16268–16292, DOI: 10.1039/D4TA02003K.

4 H. Wu, L. Wu, Y. Li, W. Dong, W. Ma, S. Li, D. Xiao, P. Huang and X. Zhang, Direct Epitaxial Growth of Polycrystalline MOF Membranes on Cu Foils for Uniform Li Deposition in Long-life Anode-free Li Metal Batteries, *Angew. Chem., Int. Ed.*, 2025, **64**(5), e202417209, DOI: 10.1002/anie.202417209.

5 J. Li, Y. Xu, W. You, C. Hong, S. Yu, Z. Ouyang, Z. Zhang, W. Yu, H. Sun, C. Yu, W. Jiang and Y. Zhou, Supramolecular Polyanions as Effective Interphase Layers for Anode-Free Lithium Metal Batteries, *Angew. Chem., Int. Ed.*, 2025, **64**(29), e202505794, DOI: 10.1002/anie.202505794.

6 Y. Chen, S. Wang, T. Wang, X. Wang, H. Sun and C. Zhu, Preparation of Cyclic Olefin Polymers via Group Transfer Radical Cyclopolymerization for High Performance in Anode-Free Batteries, *Angew. Chem., Int. Ed.*, 2025, **64**(28), e202507557, DOI: 10.1002/anie.202507557.

7 D. Aurbach, E. Zinigrad, H. Teller and P. Dan, Factors Which Limit the Cycle Life of Rechargeable Lithium (Metal) Batteries, *J. Electrochem. Soc.*, 2000, **147**(4), 1274, DOI: 10.1149/1.1393349.

8 J. Qian, B. D. Adams, J. Zheng, W. Xu, W. A. Henderson, J. Wang, M. E. Bowden, S. Xu, J. Hu and J.-G. Zhang, Anode-Free Rechargeable Lithium Metal Batteries, *Adv. Funct. Mater.*, 2016, **26**(39), 7094–7102, DOI: 10.1002/adfm.201602353.

9 M. Lei, Z. You, L. Ren, X. Liu and J.-G. Wang, Construction of copper oxynitride nanoarrays with enhanced lithiophilicity

toward stable lithium metal anodes, *J. Power Sources*, 2020, **463**, 228191, DOI: 10.1016/j.jpowsour.2020.228191.

10 N. Anansuksawat, T. Sangsanit, S. Prempluem, K. Homlamai, P. Chiochan, R. Songthan, W. Tejangkura and M. Sawangphruk, Preconcentration of lithium salt in nanoporous alumina on Cu foil as a concentrated lithium semi-solid layer for anode-free Li-metal batteries, *Chem. Commun.*, 2024, **60**(97), 14380–14383, DOI: 10.1039/D4CC03946G.

11 N. Joraleechanchai, T. Sangsanit, K. Homlamai, P. Krapong and M. Sawangphruk, Insight into the effect of thick graphite electrodes towards high-performance cylindrical Ni-rich NCA90 Li-ion batteries, *J. Energy Chem.*, 2023, **87**, 322–333, DOI: 10.1016/j.jechem.2023.08.026.

12 W. Ni, J. Lu, Y. Yang, W. Chen, Y. Fu, Z. Yuan, Y. Han and J. Wang, Research progress on diluents of localized high-concentration electrolytes for high performance lithium metal batteries, *J. Power Sources*, 2025, **640**, 236704, DOI: 10.1016/j.jpowsour.2025.236704.

13 P. Lai, B. Huang, X. Deng, J. Li, H. Hua, P. Zhang and J. Zhao, A localized high concentration carboxylic ester-based electrolyte for high-voltage and low temperature lithium batteries, *Chem. Eng. J.*, 2023, **461**, 141904, DOI: 10.1016/j.cej.2023.141904.

14 Z. Zhang, L. Hu, H. Wu, W. Weng, M. Koh, P. C. Redfern, L. A. Curtiss and K. Amine, Fluorinated electrolytes for 5 V lithium-ion battery chemistry, *Energy Environ. Sci.*, 2013, **6**(6), 1806–1810, DOI: 10.1039/C3EE24414H.

15 A. S. Keefe, S. Buteau, I. G. Hill and J. R. Dahn, Temperature Dependent EIS Studies Separating Charge Transfer Impedance from Contact Impedance in Lithium-Ion Symmetric Cells, *J. Electrochem. Soc.*, 2019, **166**(14), A3272, DOI: 10.1149/2.0541914jes.

16 Y. Lin, X. Zhang, Y. Liu, Q. Wang, C. Lin, S. Chen and Y. Zhang, Ultra-stable Li||LiFePO4 batteries via advanced designing of localized high concentration electrolyte, *J. Colloid Interface Sci.*, 2022, **628**, 14–23, DOI: 10.1016/j.jcis.2022.08.018.

17 K. Xu, M. S. Ding, S. Zhang, J. L. Allen and T. R. Jow, An Attempt to Formulate Nonflammable Lithium Ion Electrolytes with Alkyl Phosphates and Phosphazenes, *J. Electrochem. Soc.*, 2002, **149**(5), A622, DOI: 10.1149/1.1467946.

18 D.-J. Yoo, Q. Liu, O. Cohen, M. Kim, K. A. Persson and Z. Zhang, Rational Design of Fluorinated Electrolytes for Low Temperature Lithium-Ion Batteries, *Adv. Energy Mater.*, 2023, **13**(20), 2204182, DOI: 10.1002/aenm.202204182.

19 L. Le, M. Liao, A. Nguyen and D. Wang, Promoting a Stable Interface Using Localized High-Concentration Carbonate-Based Electrolyte for Li Metal Batteries, *ACS Appl. Mater. Interfaces*, 2023, **15**(31), 37497–37503, DOI: 10.1021/acsami.3c07196.

20 X. Cao, H. Jia, W. Xu and J.-G. Zhang, Review—Localized High-Concentration Electrolytes for Lithium Batteries, *J. Electrochem. Soc.*, 2021, **168**(1), 010522, DOI: 10.1149/1945-7111/abd60e.

21 T. Sangsanit, R. Songthan, S. Prempluem, W. Tejangkura and M. Sawangphruk, Stable Solid Electrolyte Interphase in Cylindrical Anode-Free Li-Metal NMC90 Batteries with Li2NiO2 Prelithiation and Fluorine-Rich Electrolytes for High Energy Density, *Nano Lett.*, 2025, **25**(22), 9047–9053, DOI: 10.1021/acs.nanolett.5c01595.

22 A. J. Louli, M. Coon, M. Genovese, J. deGooyer, A. Eldesoky and J. R. Dahn, Optimizing Cycling Conditions for Anode-Free Lithium Metal Cells, *J. Electrochem. Soc.*, 2021, **168**(2), 020515, DOI: 10.1149/1945-7111/abe089.

23 R. Weber, M. Genovese, A. J. Louli, S. Hames, C. Martin, I. G. Hill and J. R. Dahn, Long cycle life and dendrite-free lithium morphology in anode-free lithium pouch cells enabled by a dual-salt liquid electrolyte, *Nat. Energy*, 2019, **4**(8), 683–689, DOI: 10.1038/s41560-019-0428-9.

24 M. A. Zabara, G. Katırcı and B. Ülgüt, Operando Investigations of the Interfacial Electrochemical Kinetics of Metallic Lithium Anodes via Temperature-Dependent Electrochemical Impedance Spectroscopy, *J. Phys. Chem. C*, 2022, **126**(27), 10968–10976, DOI: 10.1021/acs.jpcc.2c02396.

25 H. Wan, J. Xu and C. Wang, Designing electrolytes and interphases for high-energy lithium batteries, *Nat. Rev. Chem.*, 2024, **8**(1), 30–44, DOI: 10.1038/s41570-023-00557-z.

26 E. Peled and S. Menkin, Review—SEI: Past, Present and Future, *J. Electrochem. Soc.*, 2017, **164**(7), A1703, DOI: 10.1149/2.1441707jes.

27 K.-H. Chen, K. N. Wood, E. Kazyak, W. S. LePage, A. L. Davis, A. J. Sanchez and N. P. Dasgupta, Dead lithium: mass transport effects on voltage, capacity, and failure of lithium metal anodes, *J. Mater. Chem. A*, 2017, **5**(23), 11671–11681, DOI: 10.1039/C7TA00371D.

28 C.-J. Huang, B. Thirumalraj, H.-C. Tao, K. N. Shitaw, H. Sutiono, T. T. Hagos, T. T. Beyene, L.-M. Kuo, C.-C. Wang, S.-H. Wu, W.-N. Su and B. J. Hwang, Decoupling the origins of irreversible coulombic efficiency in anode-free lithium metal batteries, *Nat. Commun.*, 2021, **12**(1), 1452, DOI: 10.1038/s41467-021-21683-6.

29 C.-J. Ko, C.-N. Tai, C.-H. Chen and K.-C. Chen, Influence of concentration-dependent diffusivity on lithium plating: Polarization, stability, and dendrite formation in phase-field simulations, *J. Energy Storage*, 2024, **97**, 112615, DOI: 10.1016/j.est.2024.112615.

30 X. Yuan, B. Liu, M. Mecklenburg and Y. Li, Ultrafast deposition of faceted lithium polyhedra by outpacing SEI formation, *Nature*, 2023, **620**(7972), 86–91, DOI: 10.1038/s41586-023-06235-w.

31 A. L. Michan, B. S. Parimalam, M. Leskes, R. N. Kerber, T. Yoon, C. P. Grey and B. L. Lucht, Fluoroethylene Carbonate and Vinylene Carbonate Reduction: Understanding Lithium-Ion Battery Electrolyte Additives and Solid Electrolyte Interphase Formation, *Chem. Mater.*, 2016, **28**(22), 8149–8159, DOI: 10.1021/acs.chemmater.6b02282.

32 R. Jung, M. Metzger, D. Haering, S. Solchenbach, C. Marino, N. Tsiouvaras, C. Stinner and H. A. Gasteiger, Consumption of Fluoroethylene Carbonate (FEC) on Si-C Composite

Electrodes for Li-Ion Batteries, *J. Electrochem. Soc.*, 2016, **163**(8), A1705, DOI: 10.1149/2.0951608jes.

33 K. Xu, Electrolytes and Interphases in Li-Ion Batteries and Beyond, *Chem. Rev.*, 2014, **114**(23), 11503–11618, DOI: 10.1021/cr500003w.

34 Y. Yamada, K. Furukawa, K. Sodeyama, K. Kikuchi, M. Yaegashi, Y. Tateyama and A. Yamada, Unusual Stability of Acetonitrile-Based Superconcentrated Electrolytes for Fast-Charging Lithium-Ion Batteries, *J. Am. Chem. Soc.*, 2014, **136**(13), 5039–5046, DOI: 10.1021/ja412807w.

35 Y. Yamada, J. Wang, S. Ko, E. Watanabe and A. Yamada, Advances and issues in developing salt-concentrated battery electrolytes, *Nat. Energy*, 2019, **4**(4), 269–280, DOI: 10.1038/s41560-019-0336-z.

36 J. Wang, Y. Yamada, K. Sodeyama, C. H. Chiang, Y. Tateyama and A. Yamada, Superconcentrated electrolytes for a high-voltage lithium-ion battery, *Nat. Commun.*, 2016, **7**(1), 12032, DOI: 10.1038/ncomms12032.

37 J. Zheng, J. A. Lochala, A. Kwok, Z. D. Deng and J. Xiao, Research Progress towards Understanding the Unique Interfaces between Concentrated Electrolytes and Electrodes for Energy Storage Applications, *Adv. Sci.*, 2017, **4**(8), 1700032, DOI: 10.1002/advs.201700032.

38 D. M. Seo, D. Chalasani, B. S. Parimalam, R. Kadam, M. Nie and B. L. Lucht, Reduction Reactions of Carbonate Solvents for Lithium Ion Batteries, *ECS Electrochem. Lett.*, 2014, **3**(9), A91, DOI: 10.1149/2.0021409eel.

39 W. M. Dose, I. Temprano, J. P. Allen, E. Björklund, C. A. O'Keefe, W. Li, B. L. Mehdi, R. S. Weatherup, M. F. L. De Volder and C. P. Grey, Electrolyte Reactivity at the Charged Ni-Rich Cathode Interface and Degradation in Li-Ion Batteries, *ACS Appl. Mater. Interfaces*, 2022, **14**(11), 13206–13222, DOI: 10.1021/acsami.1c22812.

40 R. Deng, F. Chu, F. Kwofie, Z. Guan, J. Chen and F. Wu, A Low-Concentration Electrolyte for High-Voltage Lithium-Metal Batteries: Fluorinated Solvation Shell and Low Salt Concentration Effect, *Angew. Chem., Int. Ed.*, 2022, **61**(52), e202215866, DOI: 10.1002/anie.202215866.

41 Y. Jin, N.-J. H. Kneusels, P. C. M. M. Magusin, G. Kim, E. Castillo-Martínez, L. E. Marbella, R. N. Kerber, D. J. Howe, S. Paul, T. Liu and C. P. Grey, Identifying the Structural Basis for the Increased Stability of the Solid Electrolyte Interphase Formed on Silicon with the Additive Fluoroethylene Carbonate, *J. Am. Chem. Soc.*, 2017, **139**(42), 14992–15004, DOI: 10.1021/jacs.7b06834.

42 Y. Jin, N.-J. H. Kneusels, L. E. Marbella, E. Castillo-Martínez, P. C. M. M. Magusin, R. S. Weatherup, E. Jónsson, T. Liu, S. Paul and C. P. Grey, Understanding Fluoroethylene Carbonate and Vinylene Carbonate Based Electrolytes for Si Anodes in Lithium Ion Batteries with NMR Spectroscopy, *J. Am. Chem. Soc.*, 2018, **140**(31), 9854–9867, DOI: 10.1021/jacs.8b03408.

43 B. L. D. Rinkel, J. P. Vivek, N. Garcia-Araez and C. P. Grey, Two electrolyte decomposition pathways at nickel-rich cathode surfaces in lithium-ion batteries, *Energy Environ. Sci.*, 2022, **15**(8), 3416–3438, DOI: 10.1039/D1EE04053G.

44 B. L. D. Rinkel, D. S. Hall, I. Temprano and C. P. Grey, Electrolyte Oxidation Pathways in Lithium-Ion Batteries, *J. Am. Chem. Soc.*, 2020, **142**(35), 15058–15074, DOI: 10.1021/jacs.0c06363.

45 A. J. Louli, A. Eldesoky, R. Weber, M. Genovese, M. Coon, J. deGooyer, Z. Deng, R. T. White, J. Lee, T. Rodgers, R. Petibon, S. Hy, S. J. H. Cheng and J. R. Dahn, Diagnosing and correcting anode-free cell failure via electrolyte and morphological analysis, *Nat. Energy*, 2020, **5**(9), 693–702, DOI: 10.1038/s41560-020-0668-8.

46 X. Feng, M. Ouyang, X. Liu, L. Lu, Y. Xia and X. He, Thermal runaway mechanism of lithium ion battery for electric vehicles: A review, *Energy Storage Mater.*, 2018, **10**, 246–267, DOI: 10.1016/j.ensm.2017.05.013.